

Empirically-motivated early feedback: momentum input by stellar feedback in galaxy simulations inferred through observations

Benjamin W. Keller^{*}, J. M. Diederik Kruijssen and Mélanie Chevance

Astronomisches Rechen-Institut, Zentrum für Astronomie der Universität Heidelberg, Mönchhofstraße 12-14, D-69120 Heidelberg, Germany

Accepted XXX. Received YYY; in original form 2021 September XX

ABSTRACT

We present a novel method for including the effects of early (pre-supernova) feedback in simulations of galaxy evolution. Rather than building a model which attempts to match idealized, small-scale simulations or analytic approximations, we rely on direct observational measurements of the time-scales over which star-forming molecular clouds are disrupted by early feedback. We combine observations of the spatial de-correlation between molecular gas and star formation tracers on ~ 100 pc scales with an analytic framework for the expansion of feedback fronts driven by arbitrary sources or mechanisms, and use these to constrain the time-scale and momentum injection rate by early feedback. This allows us to directly inform our model for feedback from these observations, sidestepping the complexity of multiple feedback mechanisms and their interaction below the resolution scale. We demonstrate that this new model has significant effects on the spatial clustering of star formation, the structure of the ISM, and the driving of outflows from the galactic plane, while preserving the overall regulation of the galaxy-integrated star formation rate. We find that this new feedback model results in galaxies that regulate star formation through the rapid disruption of star-forming clouds, rather than by highly efficient, global galactic outflows. We also demonstrate that these results are robust to stochasticity, degraded numerical resolution, changes in the star formation model parameters, and variations in the single free model parameter that is unconstrained by observations.

Key words: – galaxies:formation – galaxies:evolution – galaxies:ISM – galaxies:star formation – methods:numerical – ISM:bubbles

1 INTRODUCTION

Contemporary attempts to model the formation and evolution of galaxies have found that the details of the involved feedback processes are perhaps the *most* important component of both numerical and semi-analytic approaches (Somerville & Primack 1999; Scannapieco et al. 2012; Rosdahl et al. 2017). Recent simulations of star formation in giant molecular clouds (GMCs) and galaxies have included stellar winds (Rogers & Pittard 2013; Fierlinger et al. 2016; Wareing et al. 2017; Lancaster et al. 2021a), direct radiation pressure (Krumholz & Thompson 2012; Raskutti et al. 2016; Costa et al. 2018), supernovae (Keller et al. 2014; Körtgen et al. 2016; Grudić et al. 2019), photoionization (Dale 2017; Haid et al. 2019; Geen et al. 2021), as well as different combinations of these (Agertz et al. 2013; Dale et al. 2014; Grudić et al. 2021). Despite these major efforts, uncertainties in the energy losses and coupling efficiencies of these different processes have led to a situation where in some cases, very different models for stellar feedback are producing similar large-scale galaxy properties, while in other cases models including the same physical processes are producing very

different galaxies. Ideally, these processes could all be modelled from first principles. However, the computational cost of simulating the cosmological evolution of Milky Way-like galaxies with sub-pc spatial and sub- M_{\odot} mass resolution keeps this goal out of reach for the foreseeable future. Instead, we must continue to rely on approximations derived from analytic theory, high-resolution simulations of individual molecular clouds, and observational constraints. Until now, applying observational constraints has been difficult, and has been primarily relegated to post-hoc tests of simulated galaxies.

A major uncertainty in modelling stellar feedback in galaxy evolution is quantifying how efficiently feedback energy couples to the interstellar medium (ISM) to propel gas motions. The momentum generation by feedback is critical to disrupting GMCs (Murray et al. 2010; Walch et al. 2012; Kruijssen et al. 2019; Chevance et al. 2022), regulating star formation (McKee & Ostriker 1977; Gatto et al. 2017), driving turbulence in the ISM (Larson 1981; Joung & Mac Low 2006), and launching galactic outflows (Lynds & Sandage 1963; Keller et al. 2015). Unfortunately, while it is simple to derive the effect of a single feedback mechanism in toy models, the reality of multiple feedback mechanisms operating simultaneously in fractal, non-spherical GMCs greatly complicates determining how much feedback energy is converted into ISM motions.

^{*} Email: benjamin.keller ‘at’ uni-heidelberg.de

Even if the energy budget for feedback is well constrained, the momentum budget is not. Understanding how even a single feedback mechanism can interact with a turbulent, multi-phase environment can require sophisticated, ultra high-resolution simulations (Fielding et al. 2020; Lancaster et al. 2021b), which are often poorly constrained by observations, and lack the full environmental complexity of real star-forming GMCs.

With recent advances in the size and resolution of observational datasets, along with new statistical tools to understand the implications of these observations, it is now possible to directly constrain numerical models for stellar feedback via observations. On kpc scales, galaxies follow a tight, approximately linear relation between the (surface densities of the) gas mass and star formation rate (e.g. Kennicutt 1998; Bigiel et al. 2008; Leroy et al. 2008), resulting in a roughly constant molecular gas depletion time (defined as the ratio of the gas mass to the star formation rate; Bigiel et al. 2011). Schrubba et al. (2010) found that in M33 the depletion time of molecular gas depends on the scale of the aperture over which these quantities are measured. Measured depletion times diverge at smaller apertures depending on whether those apertures are centred on gas or star formation peaks. When an observational aperture is decreased below the typical separation length between independent star-forming regions (λ), gas-centred apertures will mostly contain clouds which have not yet been consumed by star formation or destroyed by feedback. Meanwhile, small apertures centred on peaks of star formation tracers ($H\alpha$ for example) are more likely to sample regions where star formation has progressed further, consuming (through star formation) and disrupting (through feedback) dense gas.

The discovery of this de-correlation between gas and young stars on small spatial scales motivated Kruijssen & Longmore (2014) (KL14 in further references) to develop an “uncertainty principle for star formation”, which is a statistical framework that uses the detailed shape of the spatial de-correlation of depletion times as a function of aperture size (the “tuning fork” diagram) to derive critical quantities for the timescale of star formation and feedback. With the method of KL14, it is now possible to systematically measure the lifetimes of molecular clouds (t_{gas}), the time-scale in which stars and gas are co-spatial (t_{FB}), the cloud-scale efficiency of star formation (ϵ_{SF}), the separation length between independent regions of the ISM (λ), and the typical size of those clouds (r_{cl}) directly from observations of star formation and dense gas (Kruijssen et al. 2018). With recent large, high resolution, high sensitivity surveys such as LEGUS (Calzetti et al. 2015), PHANGS (Lee et al. 2022; Leroy et al. 2021), and SIGNALS (Rousseau-Nepton et al. 2019), it is now possible to measure these quantities observationally across entire populations of galaxies (e.g. Kruijssen et al. 2019; Chevance et al. 2020, 2022; Ward et al. 2020; Zabel et al. 2020; Kim et al. 2021).

In this paper, we will show how these observationally-measured quantities can be used to build a new, empirically-motivated feedback (EMF) model that, by construction, applies the observational star formation and feedback timescales to determine the momentum injection rates of young massive stars. Past simulation studies (e.g. Fujimoto et al. 2019; Jeffreson et al. 2020; Semenov et al. 2021) have applied the spatial de-correlation of gas and star formation as a post-hoc test of feedback models. These works have used observations of this de-correlation to test whether their numerical models for star formation and feedback produce realistic cloud lifetimes and feedback timescales. EMF is the first stellar feedback model that uses quantities measured through observations (t_{FB} , ϵ_{SF} , and r_{cl}) as direct input parameters.

We structure the paper as follows. In Section 2, we provide a brief overview of the different mechanisms that can disrupt molecular clouds through stellar feedback. In Section 3, we show how to derive the momentum injection rate and terminal momentum from quantities measured through the KL14 method for different feedback mechanisms. This approach is used to build the EMF model, which we subsequently implement in numerical hydrodynamical simulations of galaxy evolution in Section 4. There, we present the first simulation results using this novel model for early stellar feedback, and show how this early feedback can change the mode of star formation regulation, outflow driving, and the structure of gas and stars in a Milky Way-like galaxy. We conclude with a comparison of our results to other approaches for including the effects of early stellar feedback in Section 6, and summarize our main results in Section 7.

2 FEEDBACK MECHANISMS FOR DISRUPTING MOLECULAR CLOUDS

2.1 Supernovae

Supernovae (SNe) are one of the first feedback mechanisms proposed to explain the hot galactic coronae (Spitzer 1956), observations of outflows in starburst galaxies (Lynds & Sandage 1963), and the paucity of gas in elliptical galaxies (Larson 1974). A typical core-collapse SN will release $\sim 10^{51}$ erg of energy after the death of a massive ($> 5 - 10 M_{\odot}$) star (Ekström et al. 2012). This means SNe alone produce enough energy to unbind typical Galactic-disc GMCs (Reina-Campos & Kruijssen 2017). High-resolution simulations of supernovae in molecular clouds indeed show that GMCs, after preprocessing by stellar winds or radiation, can be completely disrupted by SN feedback (Rogers & Pittard 2013).

The classic McKee & Ostriker (1977) model of a three-phase ISM relies on a hot, volume filling phase of SN-heated gas, in which cool atomic and molecular clouds reside, enveloped by an intermediate warm ionized phase. This is essentially the picture which the methodology of KL14 examines. KL14 provide a mechanism for determining the time-scale in which the cool atomic/molecular clouds are disrupted, and a characteristic separation scale of these cool clouds.

When it comes to translating the measurements made with the technique of KL14 into a physical model of feedback in the ISM, core collapse SNe (SNII) have the convenient feature of a built-in time-scale. For a given stellar population with a fully-sampled initial mass function (IMF), the first SNII will detonate ~ 3.5 Myr (Maeder & Meynet 1989; Ekström et al. 2012) after the formation of the most massive stars. This means that if the observations yield feedback time-scales shorter than this, we can rule out SNe as the mechanism for destroying star-forming clouds (Chevance et al. 2022). Uncertainty in this time-scale due to incomplete IMF sampling (Chabrier 2003; Kroupa & Weidner 2003) or the influence of binarity (Eldridge et al. 2008) or rotation (Leitherer et al. 2014) on stellar lifetimes all push this time-scale up, so 3.5 Myr is really a minimum time-scale for SN feedback. This of course also assumes that a single SN will destroy a GMC instantaneously, while in reality the expanding SN blast wave will take > 1 Myr to reach the edge of a GMC, depending on how much SN energy is lost due to radiative cooling.

Molecular cloud disruption (feedback) time-scales shorter than 3.5 Myr cannot be explained by SN feedback. As Mac Low & McCray (1988) first showed, SN detonations from sufficiently

large populations (where the number of supernovae $N_{\text{SN}} \gg 1$) can overlap and thermalize, forming a superbubble that evolves as though it were being driven by a source of constant luminosity. For typical IMFs (Kroupa 2001; Chabrier 2003), $N_{\text{SN}} \sim M_*/(100 M_\odot)$. This gives us two limits that bracket the specific energy injection by SN: an instantaneous injection of $E_{\text{SN}} = 10^{49} (M_*/M_\odot) \text{ erg}$ at 3.5 Myr, or a constant luminosity of $L_{\text{SN}} = 1.2 \times 10^{34} (M_*/M_\odot) \text{ erg s}^{-1}$ from 3.5–30 Myr.

2.2 Stellar winds

Prior to their destruction through core-collapse supernovae, massive stars inject significant energy into the surrounding natal material through line-driven stellar winds. Absorption lines from material in the outer layers of the stellar atmosphere can make that layer optically thick to those specific line frequencies (Mokiem et al. 2007). This in turn couples the photon momentum of the star's light to these outer layers, driving off a fast stellar wind ($v \sim 1000 \text{ km s}^{-1}$) which shocks the surrounding gas. This hot, over-pressured bubble will then expand into the surrounding ISM as a luminosity-driven blast wave (Weaver et al. 1977), or as a momentum-driven blast wave if radiative cooling is efficient (Lancaster et al. 2021a,b).

As stellar winds are primarily driven by metal absorption lines in their atmospheres, the total energy input from stellar winds is quite sensitive to their metallicities. Both the mass loss rates (Mokiem et al. 2007) and the terminal wind velocities (Leitherer et al. 1992) increase with greater metallicities, giving an approximately constant mechanical luminosity that depends roughly linearly on the metallicity of the star.

2.3 Direct radiation pressure

Massive stars may also inject momentum into a cloud through radiation pressure on dust and gas. Unlike stellar winds, however, there are two different mechanisms through which radiation pressure can inject energy and destroy a molecular cloud. The first is simply through the direct transfer of momentum through absorbed photons. In a medium with absorption optical depth τ_{abs} , a stellar luminosity of L injects momentum at a rate of $\dot{p} = [1 - \exp(-\tau_{\text{abs}})]L/c$. In the limit of an optically thick medium, this reduces simply to $\dot{p} = L/c$. For photon scattering, the amount of momentum injected by radiation scales proportionally to the scattering optical depth τ_{scat} , such that $\dot{p} = \tau_{\text{scat}}L/c$. This means that for sufficiently large optical depths, the coupling of photon momentum to the ambient gas is expected to be dominated by scattering rather than direct absorption.

In the case of a molecular cloud, ultra-violet (UV) photons harder than the dissociation energy of molecular hydrogen (Lyman-Werner radiation at $\sim 6\text{ eV}$) will be absorbed by H_2 molecules, breaking them apart (Christensen et al. 2012). This gives GMCs a very high optical depth to UV radiation beyond the Lyman-Werner bands, giving $\dot{p} = L_{\text{UV}}/c$ due to the UV emission of a stellar population. Dust will also absorb UV photons and re-radiate the energy imparted by the UV photons in IR bands. IR photons can then scatter on dust grains within the cloud, which in high IR optical depths leads to an enhanced momentum injection $\dot{p} = \tau_{\text{IR}}L/c$ as photons experience multiple scatterings (Krumholz & Matzner 2009).

2.4 Photoionization and HII regions

UV photons emitted by massive stars will not only impart their momentum on the gas of a cloud, but also photoionize it, breaking apart molecular gas and raising its temperature to $\sim 10^4 \text{ K}$. Early in the evolution of this ionized bubble, ionizing photons will outpace any hydrodynamic expansion of the HII region, but will rapidly reach a state where the recombination rate at the edge of the bubble matches the ionization rate set by the stellar UV flux. This transition begins once an ionization front, driven by an ionizing flux S into a medium of number density n_{H} , with a volumetric case-B recombination rate β reaches the Strömgren (1939) radius

$$r_s = \left(\frac{3S}{4\pi\beta n_{\text{H}}^2} \right)^{1/3}. \quad (1)$$

These two phases are described in the classic work of Kahn (1954) as R-type (ionization driven) and D-type (pressure driven) fronts. As the Strömgren radius in realistic clouds is significantly smaller than the cloud radius, D-type HII region expansion will be the dominant photoionization feedback for most of a GMC lifetime (this has been confirmed in 3D radiation hydrodynamic simulations of HII regions, e.g. Dale et al. 2005; Walch et al. 2012; Geen et al. 2015). If we are considering momentum generation, R-type HII fronts do not actually generate significant momentum, as they ionize gas faster than gas pressure can actually accelerate the cold, molecular gas that surrounds an ionized HII region. The dynamics of D-type HII fronts were first derived by Spitzer (1978). As the ionized interior of an HII region is overpressured, it will drive a shock into the surrounding medium, generating momentum as it sweeps up material into a shell with radius

$$r(t) \propto r_s^{3/7} t^{4/7}. \quad (2)$$

These results have been extended by Franco et al. (1990) to cover the expansion of spherically-symmetrical HII regions in clouds with a power-law density profile. Recent numerical simulations have shown that the non-spherical, turbulent structure of a GMC may have unpredictable impacts on the leakage of both ionized gas and ionizing photons from an HII region, and lower the expansion rate of a D-type HII region. Geen et al. (2018) examined clouds with identical globally-averaged properties, but with different (random) IMF sampling and turbulent driving. They find that while the average density profiles surrounding stars formed in GMCs roughly follows a power-law profile, there can be deviations of ~ 0.5 dex in the interquartile range of density at different radii. This can lead to a factor of ~ 2 scatter in momentum injected by HII regions a few Myr after star formation begins.

3 MOMENTUM GENERATION BY SELF-SIMILAR FEEDBACK FRONTS

3.1 General solution

We can begin by looking for self-similar solutions for the evolution of a feedback front. Solutions of this kind will take the form

$$r \propto t^\alpha. \quad (3)$$

We can use the cloud radius r_{cl} and the feedback time-scale t_{FB} , which is defined as the time needed for the feedback front to reach the cloud radius (Kruijssen et al. 2018), to write the dimensionless version of this proportionality as

$$\frac{r}{r_{\text{cl}}} = \left(\frac{t}{t_{\text{FB}}} \right)^\alpha. \quad (4)$$

This simple form can conveniently be used to describe a wide variety of expanding blast waves, winds, and shells. A general derivation was presented in [Ostriker & McKee \(1988\)](#) for astrophysical blast waves driven by various driving sources. As ([Ostriker & McKee 1988](#)) showed, for energy injection by a mechanical luminosity given by

$$L_{\text{in}} = L_0(t/t_0)^{\alpha_{\text{in}}-1} \quad (5)$$

the solution for α in equation (3) will depend only on the power-law exponent setting the injection rate form (α_{in}), with a functional form depending on the actual driving mechanism. For most feedback mechanisms, the specific injection luminosity for a fully-sampled IMF will be roughly constant ([Agertz et al. 2013](#)) prior to the first SN explosion, and thus we will find $\alpha_{\text{in}} = 1$ if massive star formation within a cloud occurs $\ll t_{\text{FB}}$. If this star formation continues at a constant rate for the duration of t_{FB} , we will instead have $\alpha_{\text{in}} = 2$. For an adiabatic wind, where radiative losses of the hot bubble (but not necessarily the swept-up shell) are small, we have $\alpha = (2 + \alpha_{\text{in}})/5$ ([Weaver et al. 1977](#); [Ostriker & McKee 1988](#)). If the hot bubble loses most of its thermal energy to radiation, instead we have $\alpha = (1 + \alpha_{\text{in}})/4$ ([Cioffi et al. 1988](#); [Ostriker & McKee 1988](#)). Recent studies of wind cooling in multi-phase, fractal clouds have suggested that the increased surface area of a fractal feedback front will amplify radiative cooling losses, but the expansion exponent α will still follow the overall evolution of an adiabatic or radiative shell, with the losses captured in a linear coefficient less than unity in the momentum injection rate ([Fielding et al. 2020](#); [Lancaster et al. 2021a,b](#)). Feedback fronts driven by radiation pressure will follow the evolution of radiative winds, with the same expansion exponent α as provided above. If a bubble is not driven by a thermal wind, but instead by the pressure of a photoionized HII region, [Franco et al. \(1990\)](#) showed that we can use the same self-similar solution, but this time with $\alpha = (3 + \alpha_{\text{in}})/7$. In table 1, we show the different values that the expansion exponent α can take, for different driving mechanisms with either instantaneous or constant star formation. As this table shows, the value of α is constrained to a small range $\alpha = 0.5 - 0.8$.

As the mass of the feedback front is mostly confined to the swept-up shell ([Weaver et al. 1977](#)), the mass of this shell can be written as a function of the cloud ambient density ρ_0 , feedback timescale t_{FB} , cloud radius r_{cl} , and cloud-scale star formation efficiency ϵ_{SF} , given as

$$M_s(t) = \frac{4\pi\rho_0(1 - \epsilon_{\text{SF}})r(t)^3}{3} \equiv \frac{4\pi\rho_0(1 - \epsilon_{\text{SF}})r_{\text{cl}}^3}{3} \left(\frac{t}{t_{\text{FB}}}\right)^{3\alpha} \quad (6)$$

the momentum carried by the shell will be then derived simply as the product of this equation and the time derivative of equation 4,

$$p(t) = M_s(t)v(t) \equiv \frac{4r_{\text{cl}}\alpha(1 - \epsilon_{\text{SF}})\pi\rho_0r_{\text{cl}}^3}{3t_{\text{FB}}} \left(\frac{t}{t_{\text{FB}}}\right)^{4\alpha-1} \quad (7)$$

Converting this to a specific momentum per unit stellar mass, where the stellar population mass is simply $m_* = (4/3)\pi\rho_0\epsilon_{\text{SF}}r_{\text{cl}}^3$, gives us

$$\mathbb{P}(t) = \alpha \frac{r_{\text{cl}}(1 - \epsilon_{\text{SF}})}{\epsilon_{\text{SF}}t_{\text{FB}}} \left(\frac{t}{t_{\text{FB}}}\right)^{4\alpha-1} \equiv \alpha p_0 \left(\frac{t}{t_{\text{FB}}}\right)^{4\alpha-1}, \quad (8)$$

where the second equality defines $p_0 = r_{\text{cl}}(1 - \epsilon_{\text{SF}})/\epsilon_{\text{SF}}t_{\text{FB}}$. The momentum injection rate is thus

$$\dot{\mathbb{P}}(t) = (4\alpha^2 - \alpha) \frac{p_0}{t_{\text{FB}}} \left(\frac{t}{t_{\text{FB}}}\right)^{4\alpha-2}, \quad (9)$$

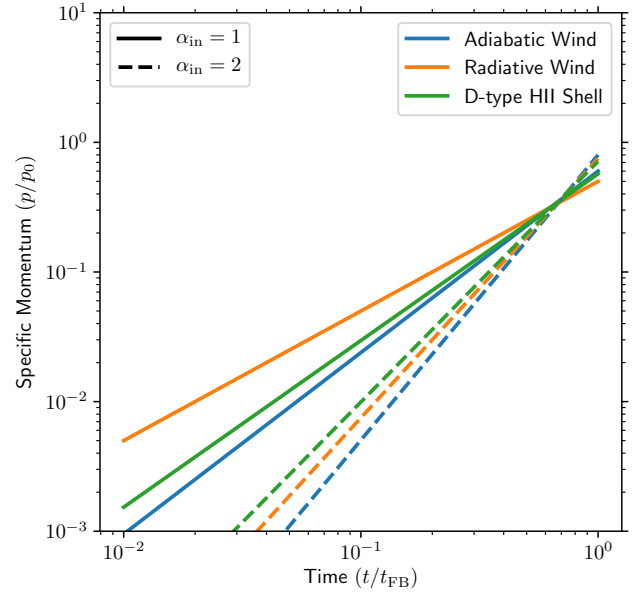


Figure 1. Momentum injected by different driving mechanisms as a function of time. As can be seen, changing the star formation from instantaneous to continuous or the mechanism driving the feedback front changes the slope of the momentum injection, but produces less than a factor of 2 difference in the final momentum injected. With instantaneous star formation, we naturally see more momentum injected earlier.

which is suitable for a direct implementation in hydrodynamical simulations of galaxy formation and evolution, once the observationally-constrained parameters p_0 and t_{FB} have been provided.

The momentum injection rates for each of the mechanisms are shown as a function of time in Figure 1. As can be seen, while the early evolution naturally is more sensitive to the uncertain driving mechanism, the constrained range of possible expansion exponents results in little variation in the final momentum injected.

3.2 Observational measurements of feedback parameters

With the equations derived in the previous section, we can construct the momentum input rate from observations of cloud radii r_{cl} , feedback time-scales t_{FB} , and star formation efficiencies ϵ_{SF} . To turn this into a two-parameter problem that only requires p_0 and t_{FB} , we use the calculation of $p_0 = r_{\text{cl}}(1 - \epsilon_{\text{SF}})/\epsilon_{\text{SF}}t_{\text{FB}}$ that is part of the HEISENBERG¹ code ([Kruijssen et al. 2018](#)), which employs a Monte-Carlo procedure to self-consistently propagate the uncertainties on p_0 .

At the time of writing, the measurements of p_0 and t_{FB} with HEISENBERG have been made for 15 nearby galaxies ([Kruijssen et al. 2019](#); [Chevance et al. 2020, 2022](#); [Ward et al. 2020](#); [Zabel et al. 2020](#); [Kim et al. 2021](#)), and will soon be extended to a total sample of > 50 galaxies (J. Kim et al. in prep.). For the purpose of this work, we use the homogeneous analysis performed on CO and H α observations of 10 nearby galaxies, published by [Kruijssen et al. \(2019\)](#) and [Chevance et al. \(2020, 2022\)](#). This sam-

¹ The code is publicly available at <https://github.com/mustang-project/heisenberg>.

Driving Mechanism	Instantaneous SF ($\alpha_{\text{in}} = 1$)	Continuous SF ($\alpha_{\text{in}} = 2$)
Adiabatic Wind; $\alpha = (3 + \alpha_{\text{in}})/5$	$\alpha = 3/5; \dot{p} \propto t^{2/5}$	$\alpha = 4/5; \dot{p} \propto t^{6/5}$
Radiative Wind; $\alpha = (2 + \alpha_{\text{in}})/4$	$\alpha = 1/2; \dot{p} \propto \text{const}$	$\alpha = 3/4; \dot{p} \propto t$
D-type HII Shell; $\alpha = (4 + \alpha_{\text{in}})/7$	$\alpha = 4/7; \dot{p} \propto t^{2/7}$	$\alpha = 5/7; \dot{p} \propto t^{6/7}$

Table 1. Self-similar expansion exponents α and the momentum injection rate for different feedback front driving mechanisms for instantaneous star formation ($\alpha_{\text{in}} = 1$) and continuous star formation. As this table shows, the range of values of α varies only slightly, from 0.5 – 0.8.

ple includes NGC300, as well as eight galaxies from PHANGS²-ALMA (Leroy et al. 2021; NGC0628, NGC3351, NGC3627, NGC4254, NGC4303, NGC4321, NGC4535, NGC5068) and one from PAWS³ (Schinnerer et al. 2013; NGC5194). For each galaxy, the measurements were made across several bins in galactocentric radius, resulting in a total of 33 independent measurements of t_{FB} and p_0 across the 10 galaxies used. For more details on the analysis, data processing, and radial binning, see Kruijssen et al. (2019) and Chevance et al. (2020, 2022).

It is plausible that t_{FB} and p_0 vary with the local properties of the GMC population and the galactic environment. However, a sample of 33 independent measurements is insufficient to definitively establish such environmental variations to the required statistical significance. Instead, this will require the same measurements to be made for the complete PHANGS sample (J. Kim et al. MNRAS submitted). Therefore, here we do not link the values of t_{FB} or p_0 to either local or galaxy-scale properties, but instead examine the effect of EMF using the averaged parameters from the current sample of 10 galaxies. This gives us median values of $t_{\text{FB}} = 3.31^{+0.83}_{-0.76}$ Myr and $p_0 = 377^{+74}_{-155}$ km s⁻¹ (where uncertainties are the 25th and 75th percentiles). The distributions of these two parameters are visualised in Figure 2.

4 NUMERICAL IMPLEMENTATION IN GALAXY SIMULATIONS

4.1 Methods and initial conditions

We implement a sub-grid model for stellar feedback based on the momentum injection rates from Section 3 into the moving-mesh semi-Lagrangian code AREPO (Springel 2010). AREPO solves Euler’s equations for hydrodynamics using the Godunov method on a Voronoi mesh generated on-the-fly using mesh generating points that follow the fluid flow in each cell. This method allows for low dissipation and second-order spatial integration accuracy through the use of a Riemann solver to calculate fluxes between Voronoi cells, while maintaining Galilean invariance.

AREPO has been applied to study galaxy formation in large-volume cosmological simulations (Vogelsberger et al. 2014), cosmological zooms of individual galaxies (Grand et al. 2017), isolated galaxies (Smith et al. 2018), and stratified slices of the ISM (Simpson et al. 2016). Radiative cooling in our version of AREPO is handled by the GRACKLE 3.1 (Smith et al. 2017) cooling library, which allows us to include primordial & metal line cooling using tabulated CLOUDY (Ferland et al. 2013) rates. We use GRACKLE in equilibrium mode with an initial ISM metallicity of

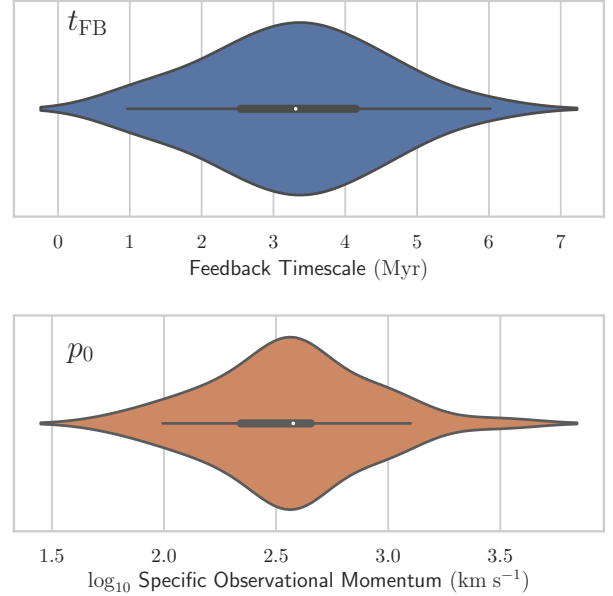


Figure 2. Violin plots of the two observationally-constrained parameters in EMF, t_{FB} (top panel) and p_0 (bottom panel). The coloured regions show a kernel density estimate of the observed values. The thick inner lines connect the upper and lower quartiles, while the thin lines show the full extents of the measurements. The white points in the centres show the median values ($t_{\text{FB}} = 3.3$ Myr and $p_0 = 377$ km s⁻¹, respectively).

$Z = 0.012$. The UV background used in these simulations is derived from Haardt & Madau (2012), at $z = 0$. We also include a non-thermal pressure floor to ensure that the Truelove et al. (1997) criterion is not violated, preventing numerical fragmentation at the resolution scale. Star formation in our simulations uses a standard Schmidt-law prescription, with stars forming from gas cells at a rate set by $\dot{\rho}_* = \epsilon_{\text{ff}} \rho / t_{\text{ff}}$, where t_{ff} is the gas free-fall time, and ϵ_{ff} is the dimensionless star formation efficiency (per free-fall time) parameter. We allow gas cells with density above 100 cm^{-3} and temperature below 10^4 K form stars, with a local star formation efficiency per free-fall time of $\epsilon_{\text{ff}} = 0.1$. While this value is near the upper range of observed cloud-scale star formation efficiencies (Evans et al. 2009; Heyer et al. 2016; Grudić et al. 2019), it should be noted that the efficiency of the sub-grid star formation model ϵ_{ff} does not account for the effect of feedback (which we explicitly model in our simulations). The actual cloud-scale star formation efficiency in these simulations are therefore an emergent property of gravity, hydrodynamics, and feedback in concert (e.g. Grisdale et al. 2019).

We simulate an isolated, Milky-Way like galaxy with initial conditions (ICs) drawn from the AGORA comparison project (Kim et al. 2014). The AGORA isolated disc IC has a disc scale radius of 3.43 kpc and a scale height of 343 pc. The disc is embedded in

² PHANGS is Physics at High Angular Resolution in Nearby Galaxies, more information is available at <http://phangs.org>

³ PdBI Arcsecond Whirlpool Survey, <https://www2.mpa-hd.mpg.de/PAWS/PAWS/Home.html>.

a dark matter (DM) halo with a mass of $M_{200} = 1.07 \times 10^{12} M_{\odot}$ and a virial radius of $R_{200} = 205$ kpc. The halo concentration parameter is $c = 10$, with a [Bullock et al. \(2001\)](#) spin parameter of $\lambda = 0.04$. The galaxy model contains both a stellar disc and bulge, with a bulge-to-disc ratio of 0.125 and a total gas fraction of 0.18. The AGORA disc ICs were generated using the MAKE-NEWDISK code ([Springel et al. 2005](#)). We use a gravitational softening length of 40 pc and 260 pc for baryons and DM respectively, and a gas cell mass of $8.59 \times 10^3 M_{\odot}$. In Appendix A, we show that the star formation and feedback quantities we measure here are well-converged at this resolution. The IC star particle mass is $3.437 \times 10^4 M_{\odot}$, and the live DM halo contains 10^5 particles of mass $1.254 \times 10^6 M_{\odot}$ each. We use Lagrangian refinement to ensure that individual cell masses never deviate by more than a factor of two from the target mass resolution. We initialize the gas in the simulation with a temperature of 10^4 K, though this is rapidly replaced with the equilibrium temperature calculated by GRACKLE.

4.2 Numerical implementation of empirically-motivated early feedback

We implement EMF as a model with three parameters. The first two are t_{FB} and $p_0 = r_{\text{cl}}(1 - \epsilon_{\text{SF}})\epsilon_{\text{SF}}^{-1}t_{\text{FB}}^{-1}$ and are constrained empirically, while the third parameter is α , which needs to be chosen from a range of possible values (see table 1). Following equation (8), during a timestep Δt star particles with birth mass M_i and age $t < t_{\text{FB}}$ will inject an amount of momentum

$$\Delta p(M_i, t, \Delta t) = \alpha p_0 M_i \left[\left(\frac{t + \Delta t}{t_{\text{FB}}} \right)^{4\alpha-1} - \left(\frac{t}{t_{\text{FB}}} \right)^{4\alpha-1} \right]. \quad (10)$$

Naturally, this is a piecewise linear approximation of the momentum injection rate of equation (9). The momentum generated by each star particle is deposited into the surrounding cells by first finding the cell in which a star particle resides, and using the Voronoi mesh to weight the contribution to each of the cells by their relative area. Any momentum cancellation that occurs due to existing motions of the surrounding gas cells is thermalized, and this thermal energy is deposited in the star particle's host cell. The cell that a star particle resides in has a total surface area A_i , and its cell faces shared with each surrounding cell contribute an area S_j , such that $A_i = \sum_j S_{ij}$, giving a weight of $W_{ij} = S_{ij}/A_i$ for each neighbouring cell. Thus, each star particle contributes to a cell j momentum $p_j = p(M_i, t, \Delta t)W_{ij}$, in the direction of the normal vector to the surface S_{ij} . This guarantees that the total *absolute* momentum injected is $p(M_i, t, \Delta t)$, while the total vector momentum is zero by the divergence theorem (thus ensuring momentum conservation). This algorithm can be trivially adapted for both fixed-mesh Eulerian codes and Smoothed-Particle Hydrodynamics (SPH) Lagrangian codes, simply by replacing the weighting factor $w_j = S_j/A$ with the Cartesian equivalent or an SPH kernel weight.

As discussed in Section 3.2, the parameters p_0 and t_{FB} are derived from the observational data ($p_0 = 377 \text{ km s}^{-1}$, $t_{\text{FB}} = 3.3 \text{ Myr}$). As the exponent α is unconstrained observationally, arising from the density structure of GMCs and the feedback driving mechanism, we simulate cases with two different values of $\alpha = \{0.5, 1.0\}$. This range bounds all reasonable possible values of α , as shown in Table 1 and discussed in Section 3.

Supernova feedback is handled by the mechanical supernovae scheme first described in [Kimm & Cen \(2014\)](#), using the same

Voronoi face weighting scheme as the EMF. In brief, we calculate a terminal momentum, when a single SN transitions to the momentum-conserving phase

$$\frac{p_{\text{term}}}{10^5 \text{ km s}^{-1} M_{\odot}} = 3E_{51}^{16/17} n_H^{-2/17} \max(Z/Z_{\odot}, 0.01)^{-0.14}. \quad (11)$$

In this equation, E_{51} is the total energy of all SN detonating within a cell (in units of 10^{51} erg), while n_H is the ambient density of each cell momentum is injected into. The mechanical feedback algorithm then automatically switches between a thermal-dominated and kinetic-dominated algorithm based on the local resolution. Of the total SN energy E_{SN} injected into cell i , we deposit kinetic energy into neighbouring cells j in the form of momentum, calculated as

$$p_{\text{FB}} = \min(\sqrt{2W_{ij}M_jE_{\text{SN}}}, W_{ij}p_{\text{term}}). \quad (12)$$

Each cell always deposits a total energy of E_{SN} , with the kinetic fraction set by p_{FB} . Kinetic energy is injected into the neighbouring cells, while the thermal fraction is deposited into the central cell. Thus, if M_j is large (in the limit of low resolution), we inject the terminal momentum, leading to a small thermal contribution, while if M_j is small (in the limit of high resolution), we inject a larger fraction as thermal energy, which then will generate the terminal momentum self-consistently through gas pressure acting on the surrounding material. This method is similar to [Hopkins et al. \(2018a\)](#) and [Smith et al. \(2018\)](#), and has been used by [Jefreson et al. \(2020, 2021a,b\)](#) and [Keller & Kruijssen \(2022\)](#). We deposit 10^{51} erg per SN and calculate the chemical enrichment using a physically-motivated SN distribution generated by SLUG⁴ ([Krumholz et al. 2015](#)), using rate tables drawn from [Sukhbold et al. \(2016\)](#). In addition to core-collapse SNI, we also deposit mass, metals, and energy from SNIa using a delay-time distribution derived by [Maoz et al. \(2012\)](#) with metal yields from [Seitenzahl et al. \(2013\)](#).

In Figure 3, we show the specific momentum injected from a stellar population by both EMF and SN. As can be seen, the total momentum injected by EMF with $\alpha = 1.0$ is roughly twice the total momentum injected with $\alpha = 0.5$, though most of this momentum is injected later, only exceeding the momentum injected with $\alpha = 0.5$ after 2 Myr. The momentum injected by SN is calculated using equation 11 in an ambient ISM with $n_H = 1 \text{ cm}^{-3}$ and solar metallicity. While this likely overestimates the momentum budget of SN at early times, it represents the final momentum that will be injected at the end of the pressure-driven snowplow phase ([Cioffi et al. 1988](#); [Blondin et al. 1998](#)). As can be seen in Figure 3, the terminal SN momentum is 5-10 times larger than the momentum injected by EMF, but this momentum only begins being deposited after ~ 3 Myr. EMF modifies the timing of momentum injection, without significantly changing the total momentum injected by all forms of feedback after the final SN detonates.

5 IMPACT OF EMPIRICALLY-MOTIVATED FEEDBACK ON GALACTIC STRUCTURE AND THE MULTI-SCALE BARYON CYCLE

In this section, we discuss how our new empirically-motivated feedback model influences the baryon budget of galaxies through

⁴ Stochastically Lighting Up Galaxies, <https://slug2.readthedocs.io/en/latest/>.

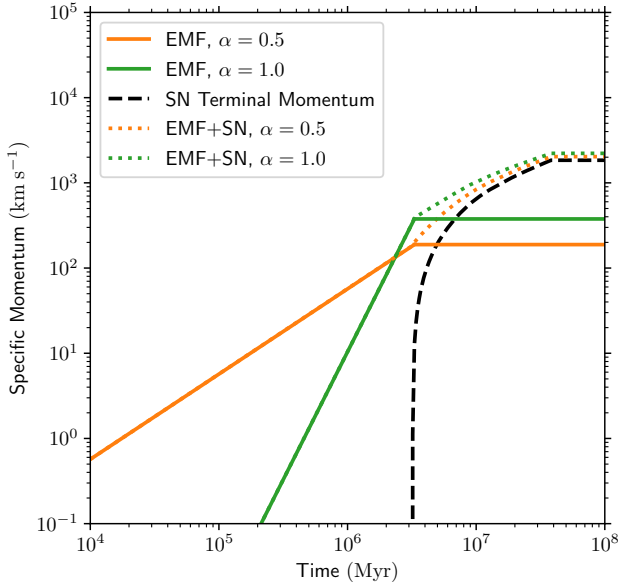


Figure 3. Total specific momentum injected by SN (black curve) and EMF with $\alpha = 0.5$ (orange curve) and $\alpha = 1.0$ (green curve). The SN momentum is calculated using equation 11, along with SN rates calculated by STARBURST99 for a fully-sampled Kroupa (2001) IMF, in an ambient medium with $n_H = 1 \text{ cm}^{-3}$ and solar metallicity. The coloured dashed curves show the momentum injected by both EMF and SN together.

the balance between star formation and outflows, how it affects the structure and properties of the galactic disc, and how it impacts the molecular cloud lifecycle. Taken together, this describes how the multi-scale baryon cycle changes when adding EMF.

5.1 Self-Regulation and Outflows

The first question we examine is how the addition of EMF changes the overall regulation of star formation, which is often tied together with the ability of star formation to drive outflows from the galactic disc (Keller et al. 2015; Rosdahl et al. 2017). In Figure 4, we examine the star formation rate \dot{M}_* , the gas outflow rate \dot{M}_{out} , and the mass loading ($\eta = \dot{M}_{\text{out}}/\dot{M}_*$) for a galaxy simulated with SN feedback alone, versus two cases of EMF with $\alpha = \{0.5, 1.0\}$. Outflow rates are calculated in the direction perpendicular to the disc plane, through two 500 pc thick slabs located 5 kpc above and below the disc mid-plane. We also smooth the outflow rates over a 10 Myr window to remove the high-frequency stochasticity in the outflow rate.

After a ~ 400 Myr settling period, during which the disc cools and comes into feedback self-regulation, the star formation rates (SFRs) of the simulated galaxies are comparable, with a relatively constant SFR of $\sim 3 \text{ M}_\odot \text{ yr}^{-1}$ in the SN only case, and a slowly declining SFR from $\sim 6 \text{ M}_\odot \text{ yr}^{-1}$ at 400 Myr to $\sim 3 \text{ M}_\odot \text{ yr}^{-1}$ at 1 Gyr in the galaxies simulated with EMF.⁵ As we might expect, EMF reduces the magnitude of the initial starburst, which is

⁵ Interestingly, the reduced initial burst of star formation when early feedback is included has also been seen in extremely high resolution simulations of dwarf galaxies by Smith et al. (2021). Despite only lasting 4 Myr, the initial delay between the first stars forming and SN feedback occurring appears to be enough to push the disc out of equilibrium in isolated galaxy simulations, independently of the mass scale and resolution.

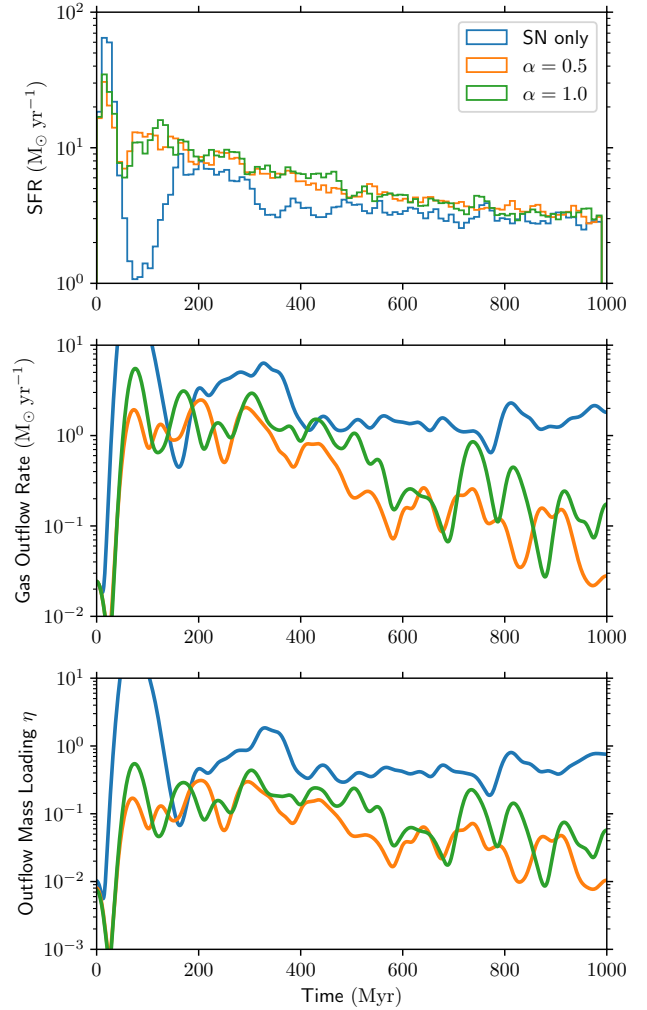


Figure 4. Star formation rate (top panel), outflow rate (middle panel), and mass-loading (bottom panel) for three different isolated disc galaxies (one with SN feedback only and two including EMF with $\alpha = \{0.5, 1.0\}$). As the top panel shows, after an initial burst of star formation and settling of the disc, the final 500 Myr of evolution for all three examples show roughly equivalent star formation rates. However, the outflow rates and mass loadings are approximately an order of magnitude lower with the addition of EMF.

triggered by the disc cooling out of equilibrium before SN feedback regulation can moderate the SFR. Without any form of early feedback, the SN-only run is able to form stars in newly collapsed GMCs for ~ 4 Myr prior to any feedback energy being injected, which greatly amplifies the initial burst. After 1 Gyr, the final stellar mass of the galaxy is $3.32 \times 10^9 \text{ M}_\odot$ in the SN-only case, versus $\{4.03, 4.21\} \times 10^9 \text{ M}_\odot$ for $\alpha = \{0.5, 1.0\}$. EMF modestly increases the averaged star formation rate by $\sim 20\%$ over simulations with SN alone, which is in part caused by the different response to the initial starburst. For the final 200 Myr, long after the effects of the initial starburst have receded, the average SFR for the SN-only case is $2.89 \text{ M}_\odot \text{ yr}^{-1}$, versus $\{3.33, 3.24\} \text{ M}_\odot \text{ yr}^{-1}$ for $\alpha = \{0.5, 1.0\}$, a difference of only 11 – 14%.

In contrast with the SFRs and stellar masses, the outflow rates exhibit two major quantitative differences. First, EMF produces a significantly reduced average outflow rate and mass loading. For SN feedback alone, the median outflow rate for the final 500 Myr

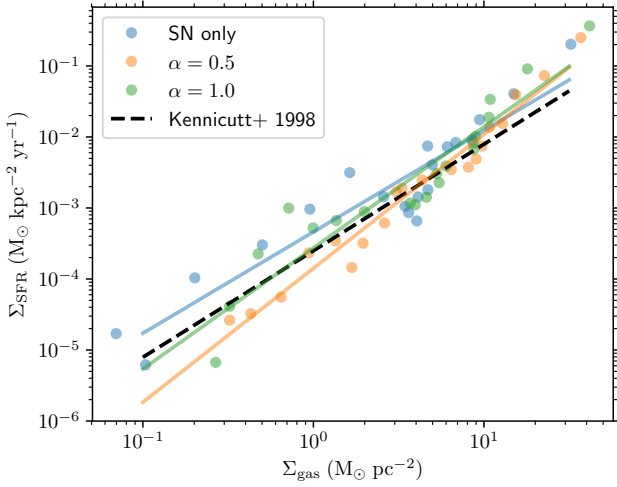


Figure 5. Kennicutt-Schmidt diagram showing the relation between total gas surface density Σ_{gas} and star formation surface density Σ_{SFR} in our simulated galaxies with SN alone (blue points) and EMF with $\alpha = 0.5$ (orange points) and $\alpha = 1.0$ (green points). Solid curves show power-law fits to each set of data points. The dashed line shows the Kennicutt (1998) observational relation. We see a slightly lower Σ_{SFR} for the galaxies which include EMF when $\Sigma_{\text{gas}} < 1 \text{ M}_{\odot} \text{ pc}^{-2}$, and steeper slopes to the fitted Kennicutt-Schmidt relations for the EMF galaxies.

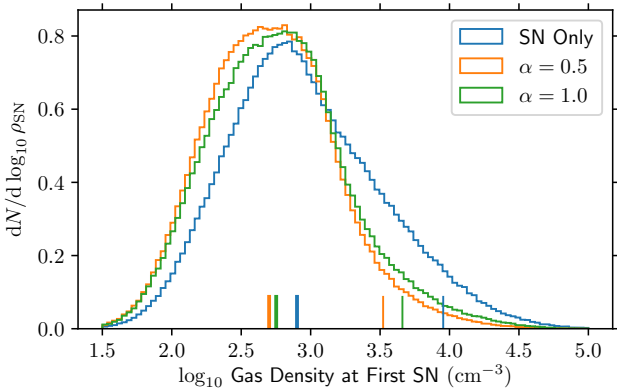


Figure 6. Probability distribution function of the ambient gas density at the location of the first SN event of each star particle, for three simulated galaxies (one with SN feedback only and two using EMF with $\alpha = \{0.5, 1.0\}$). The thick vertical markers show the median gas densities at the first SN event, and the thin vertical markers show the 95th percentiles, probing the SNe that detonate in the densest environments (where they will suffer most from radiative cooling). As is clear, EMF reduces the typical ISM density that SNe detonate within, and in particular it shifts the high-density tail of the SN environmental density, lowering the 95th percentile by a factor of 2–3.

of the simulation is $1.4 \text{ M}_{\odot} \text{ yr}^{-1}$, while EMF drives median outflow rates of $\{0.11, 0.20\} \text{ M}_{\odot} \text{ yr}^{-1}$ for $\alpha = \{0.5, 1.0\}$. Not only is the averaged outflow rate (and mass loading) reduced by roughly a factor of 10 when EMF is enabled, these outflows also become more transient, with variations of ~ 1 dex over $\sim 50 - 100$ Myr time-scales. This may indicate a greater sensitivity to the local ISM environment in the simulations which include EMF. Past studies Rosdahl et al. (2017); Keller & Kruijssen (2022) have shown that the detailed modelling of stellar feedback produces a more signifi-

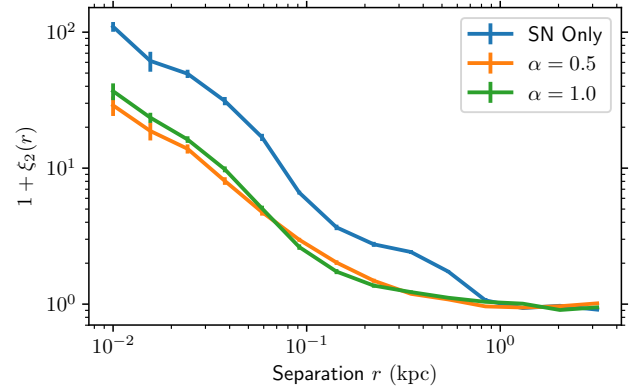


Figure 7. Two-point correlation function of young (< 20 Myr) stars, for three simulated galaxies (one with SN feedback only and two including EMF with $\alpha = \{0.5, 1.0\}$). While there is no statistically significant difference between the small-scale (< 100 pc) correlation of young stars for different values of α , the clustering of stars in the run without early feedback is much larger on scales below 1 kpc.

cant impact on outflow rates than the SFR, though the magnitude of the effects depends on the feedback process and numerical model being considered.

In the Kennicutt-Schmidt diagram shown in Figure 5, we calculate gas and SFR surface density at $t = 1$ Gyr in 20 radial annuli of 1 kpc width between 0 – 20 kpc, excluding gas which is more than 1.5 kpc above the galaxy midplane. The star formation rates here are calculated using stars younger than 50 Myr. We can see that the three cases (SN alone, EMF with $\alpha = 0.5$, and EMF with $\alpha = 1.0$), the general trend follows the Kennicutt (1998) relation for $\Sigma_{\text{gas}} < 10 \text{ M}_{\odot} \text{ pc}^{-2}$, but increases in slope at higher gas surface densities. We see a somewhat higher Σ_{SFR} at low gas surface density ($\Sigma_{\text{gas}} < 1 \text{ M}_{\odot} \text{ pc}^{-2}$) when EMF is omitted. The best-fit Kennicutt-Schmidt relations ($\Sigma_{\text{SFR}} = A(\Sigma_{\text{gas}}/\text{M}_{\odot} \text{ pc}^{-2})^N \text{ M}_{\odot} \text{ kpc}^{-2} \text{ yr}^{-1}$) for each case is $A = 4.6 \times 10^{-4}$, $N = 1.4$ for SN alone; $A = 1.4 \times 10^{-4}$, $N = 1.9$ for EMF with $\alpha = 0.5$, and $A = 2.7 \times 10^{-4}$, $N = 1.7$ for EMF with $\alpha = 1.0$. With a different number of annuli or pixel-based Kennicutt-Schmidt surface densities, we see the same general trend: higher SFR at low surface densities for SN alone, and a steeper best-fit Kennicutt-Schmidt relation with EMF included.

It may seem puzzling at first that including additional feedback momentum from pre-SN feedback would reduce the overall effectiveness of stellar feedback to drive mass-loaded galactic winds and fountains. To understand this, we need to examine the environment in which the SNe detonate. Early feedback can change the efficiency of star formation regulation through three channels: adding to the overall energy and momentum budget, changing the ambient density in which SN detonate (thereby changing cooling losses), and changing the spatial and temporal clustering of SNe. In Figure 6, we show how the ambient gas density around the first SN event changes with the addition of EMF. We measure the ambient density as the density of the gas cell in which a star particle finds itself at the time of the first SN event. By measuring the ambient density of the first SN event, rather than for all SNe that are produced by a star particle, we isolate how EMF shapes the initial gas environment that SNe may detonate in, because the first SN events may change the detonation environment of later SNe. As can be seen from the histogram in Figure 6, EMF causes a slight reduction of the median density that SNe detonate in. For

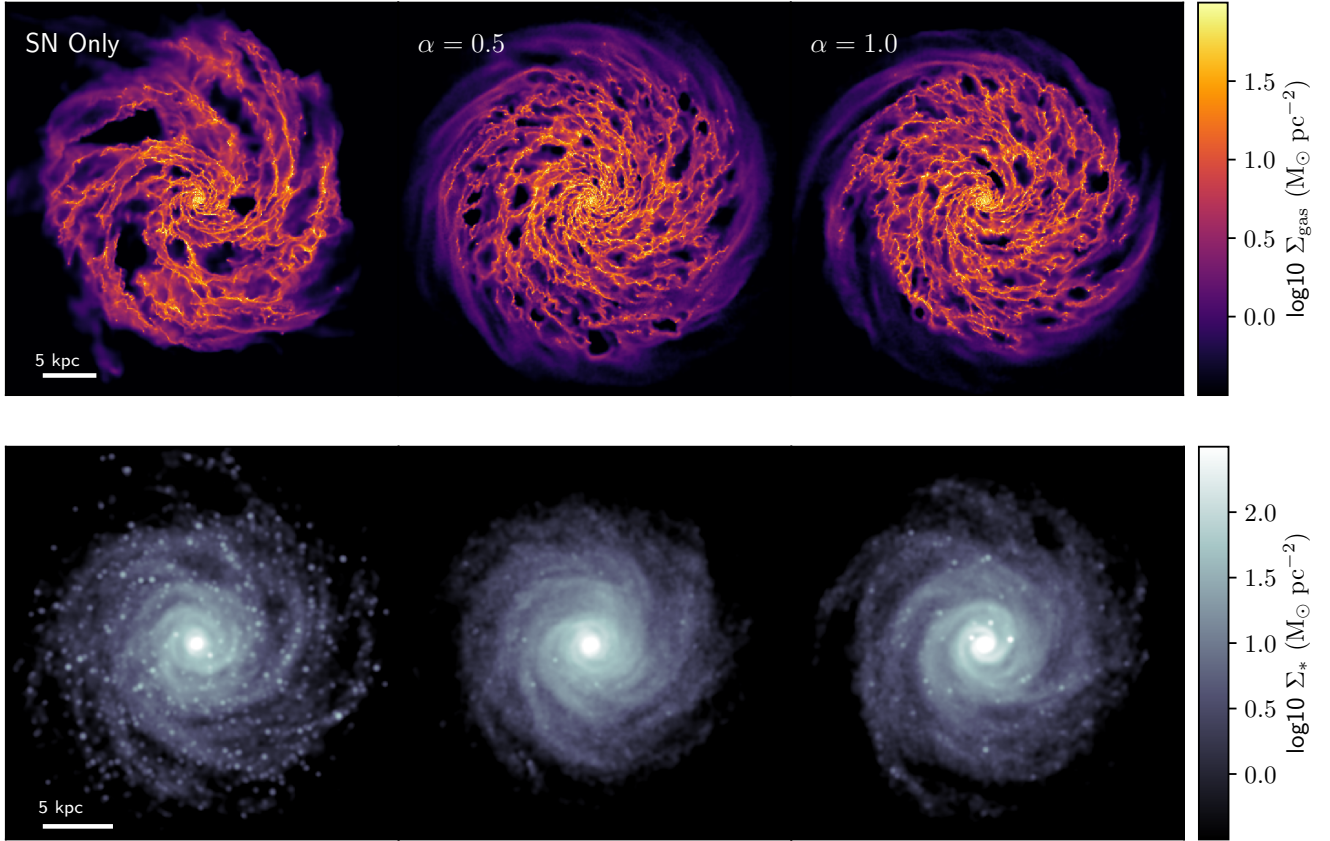


Figure 8. Gas (top row) and stellar (bottom row) column density maps at $t = 1$ Gyr for an isolated disc galaxy with SN feedback only (leftmost panel), and when including EMF with $\alpha = \{0.5, 1.0\}$ (see the annotations). The ISM is more homogeneous and flocculent when EMF is included. Feedback-driven voids in the ISM are generally smaller, and the spiral arm structure is less pronounced. In the stellar column density, the EMF simulations clearly show reduced small-scale clustering, with only a handful of dense stellar groups visible in each of the EMF cases. The top panels have a width of 40 kpc, while the bottom panels have a width of 30 kpc.

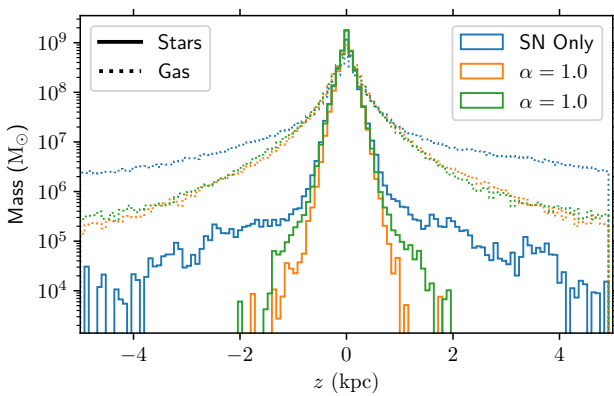


Figure 9. Vertical profiles of gas (dotted curves) and stars (solid curves) for each of our simulated galaxies. As before, we see little difference between different values of α when EMF is included, but there is a notable decrease in gas at high latitudes relative to the SN-only simulation. This is to be expected from the reduced outflow rates, because the isolated nature of these discs implies that gas significantly above the initial scale height of 343 pc is deposited there primarily through outflows. Interestingly, we also see a significant, highly extended thick stellar disc component in simulations without EMF. With EMF included, no stars are found more than ~ 2 kpc above or below the disc.

SNe alone, the median gas density at the site of the first SN event is $8.0 \times 10^2 \text{ cm}^{-3}$, compared to $\{5.0, 5.7\} \times 10^2 \text{ cm}^{-3}$ when including EMF with $\alpha = \{0.5, 1.0\}$. The high-density tail, where SN will experience the most extreme cooling losses, shows a somewhat stronger trend. Without EMF, the 95th-percentile ambient density is $9.0 \times 10^3 \text{ cm}^{-3}$, versus $\{3.3, 4.6\} \times 10^3 \text{ cm}^{-3}$ when including EMF with $\alpha = \{0.5, 1.0\}$. These results alone should point to *greater* efficiency for stellar feedback to drive outflows and regulate star formation, as lower ambient densities at the site of SN detonation should yield less radiative losses, and allow more energy to drive gas heating and acceleration.

Figure 6 shows that the reduced outflow rates cannot be explained by a change in the overall cooling losses of the first SN that might have been driven by early feedback expelling gas from the SN environment. However, it has also been shown that clustered SN are much more efficient at injecting momentum (Gentry et al. 2020) and driving galactic outflows (Fielding et al. 2018; Martizzi 2020). In Figure 7, we show the two-point correlation function, calculated with the Landy & Szalay (1993)⁶ estimator, of young (with

⁶ The Landy & Szalay (1993) estimator uses the number of true pairs within a separation r , $DD(r)$, together with the number of random pairs with the same mean density $RR(r)$ and the cross-correlated data-random pairs $DR(r)$ to calculate $\xi_2(r) = (DD(r) - 2DR(r) + RR(r))/RR(r)$.

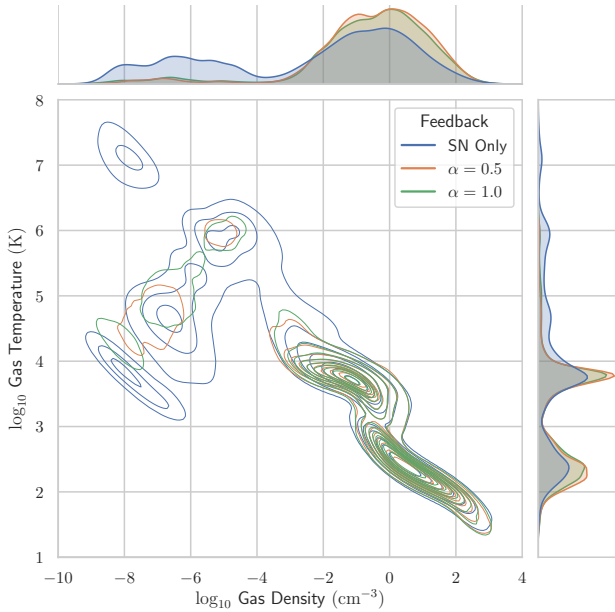


Figure 10. Density-temperature phase diagram for three simulated galaxies (one with SN feedback only and two including EMF with $\alpha = \{0.5, 1.0\}$). Each panel shows a kernel density estimate (KDE) weighted by gas mass, for each simulated galaxy. The central panel shows contours of this KDE in the density-temperature plane, while the marginal panels each show the probability distribution function in density (top panel) and temperature (right panel). Each contour set contains ten equally spaced quantiles from 0.05 to 1 in the KDE probability. As can be seen, there is little difference in the distribution of gas in either density or temperature as a function of α . However, when only including SN feedback, we see significantly more gas at high ($> 10^5$ K) temperatures and low densities ($< 10^3$ cm $^{-3}$). This is a result of the reduced radiative losses that occur due to the clustering of SN feedback demonstrated in Figure 7.

ages < 20 Myr) stars in each of our simulations. As can be seen, on length scales below 800 pc, the galaxy simulated with SN feedback alone exhibit a significantly enhanced clustering of young star particles. The probability of finding pairs of star particles with separations of ~ 10 pc is up to 4 times greater when EMF is omitted. This difference follows naturally from the delay of stellar feedback in the SN-only simulation. SN feedback begins 4 Myr after the birth of a star particle, which corresponds to the typical main sequence lifetime of the most massive ($> 40 M_{\odot}$) stars. This allows additional star formation in the neighbourhood of young star particles to continue unopposed by the injection of feedback from star particles that have already formed, but that have not yet detonated their first SN. By contrast, EMF regulates star formation on the cloud scale during the ~ 3 Myr after the first star particle forms, thereby reducing the overall clustering of young stars and diminishing the effectiveness of SNe at driving galactic outflows. The same effect has been seen in the recent, high-resolution dwarf galaxy simulations of Smith et al. (2021). Despite a ten-fold reduction in galactic outflows, this local (rather than global) regulation of star formation produces an averaged galactic SFR that is nearly indistinguishable from the SN-only case.

The Landy & Szalay (1993) estimator is designed to minimize errors occurring from a non-periodic distribution of points.

5.2 How EMF reshapes the stellar and gaseous discs

So far, we have demonstrated changes in the mode of star formation regulation by the addition of early feedback. Without early feedback, star formation shows stronger spatial correlation, which in turn produces larger SN-powered superbubbles, driving higher outflow rates and producing larger voids in the ISM. This changing mode of regulation produces both quantitative and qualitative differences in the structure of the ISM and the stellar discs of our simulated galaxies. The qualitative changes are clearly illustrated in Figure 8, where we show maps of the stellar and gas surface densities. In the gas surface density maps, the ISM shows significantly different structure with EMF included. With SN feedback alone, the ISM is organised around a handful of large, feedback-driven voids in the inter-arm regions of the galactic disc. When EMF is included, the disc becomes more uniform, with less prominent spiral arms and a more flocculent morphology. The stellar column density map illustrates qualitatively what we previously quantified in Figure 7. EMF significantly reduces the number of small, dense stellar groups, resulting in a disc that is smoother and more uniform. The handful of stellar groups that remain are found primarily along spiral arms, with very few lying in either the interarm regions or the outskirts of the stellar disc.

Differences in the spatial distribution of gas and stars, like those seen in the face-on projections of Figure 8, also exist in the vertical structure of our simulated galaxies. In Figure 9, we show the z -axis mass distribution of gas and stars in galaxies simulated with and without empirically-motivated feedback. As would be expected from the higher outflow rates of the SN-only simulation, its vertical gas profile has much more mass outside the gaseous disc ($|z| \gtrsim 1$ kpc) than the simulations with EMF. Another interesting side-effect of the more vigorous, SN-stirred ISM is the presence of stars at high galactic elevations in the SN-only simulation. When EMF is included, the stellar disc truncates completely at $|z| \sim 2$ kpc. When this early feedback is omitted, we find broad wings of stellar mass, extending even beyond $|z| \sim 4$ kpc. These stars may be kicked to higher orbits by forming in gaseous regions with large σ_z , through dynamical interactions, or may have formed in dense gas entrained along with outflows (Yu et al. 2020). Of course, it is important to realise that the stellar population outside of the plane in real-Universe galaxies is mostly shaped by satellite galaxy accretion (e.g. Helmi et al. 2018; Kruijssen et al. 2020; Naidu et al. 2021). Therefore, we leave further investigation of this phenomenon to a future study that will include the effects of the cosmological environment on the shaping of the halo star population.

In Figure 10, we show the impact of EMF on the physical state of the gas in our simulated galaxies, visualised in the density-temperature plane. The typical features of a three-phase ISM are seen both in the simulations with and without EMF. A hot phase evolves adiabatically as it leaves the disc, a warm ionized or neutral phase is found between 10^3 – 10^4 K, which exists in rough pressure equilibrium with a cool neutral phase between 10 and a few 100 K. As the contours show, the cool phase is mostly isobaric ($\rho T \approx \text{const}$), while the warm phase shows a shallower slope, closer to (but not fully) being isothermal. This shallow, pseudo-isothermal profile is simply a result of the ionizing UV background. The temperature and density histograms along the horizontal and vertical edges of Figure 10 clearly show the quantitative differences between the simulations with only SN feedback and those that include EMF. As can be seen, the relative amount of hot, diffuse gas is significantly higher for SN feedback alone than when

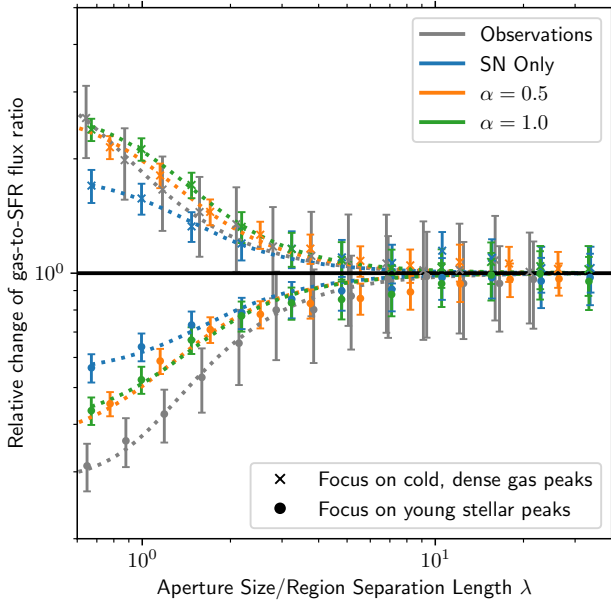


Figure 11. Tuning fork diagram for observations of the LMC along with our three simulated galaxies. The horizontal axis shows the aperture size over which gas and young stellar fluxes are measured, normalized to the inferred region separation length λ . The vertical axis shows the ratio of the gas to young stellar (SFR) fluxes, normalized to the global average ratio. The upper arm of the tuning fork shows measurements where apertures are centred on gas peaks, while the lower arm shows measurements where the apertures are centred on young stellar peaks. As can be seen, the simulations with SN feedback alone show a smaller, more flattened opening on small scales, while simulations that include EMF show an opening comparable to the tuning fork observed for the LMC (Ward et al. 2020; Kim et al. 2021).

EMF is included. The total mass of gas above 10^4 K with SN only is $1.9 \times 10^9 M_\odot$, compared to $\{3.9, 4.6\} \times 10^8 M_\odot$ when including EMF with $\alpha = \{0.5, 1.0\}$. This is another manifestation of the enhanced efficiency of SN feedback seen previously in Figure 4, driven by the enhanced clustering shown in Figure 7. We verify that the changes we see in star formation regulation and the ISM phase distribution are robust to galactic stochasticity (Keller et al. 2019) in Appendix B.

5.3 Spatial de-correlation of gas and stars

The observationally-derived quantities we have used for our EMF simulations were determined by Kruijssen et al. (2019) and Chevance et al. (2020, 2022), who analysed the spatial de-correlation of gas and stars down to $\lesssim 100$ pc scales in 10 nearby galaxies, using the HEISENBERG code (Kruijssen et al. 2018). In this section, we analyse our simulated galaxies with the same methodology, to reveal how EMF changes the spatial de-correlation of star-forming gas and young stars. In order to do this, we generate mock surface density maps of star-forming gas and young stars. For the gas maps, we use all gas cells with densities above our star formation threshold, 100 cm^{-3} . For the young stars, we select all stars with ages below 10 Myr. We then generate 20×20 kpc column density maps, with a resolution of 1000×1000 pixels (such that each pixel corresponds to 20 pc). We then smooth the images with a Gaussian beam with $\sigma = 20$ pc (or a full width half maximum of ~ 50 pc), comparable to the size of the resolution element of the observations analysed by Kruijssen et al. (2019) and Chevance

Galaxy	t_{gas} (Myr)	t_{FB} (Myr)
LMC (observations)	$11.1^{+1.6}_{-1.7}$	$1.1^{+0.3}_{-0.2}$
PHANGS++ (observations)	19.8 ± 6.1	3.3 ± 1.2
SN Only	$14.8^{+1.7}_{-1.5}$	$3.3^{+0.7}_{-0.7}$
EMF $\alpha = 0.5$	$10.7^{+0.9}_{-0.8}$	$2.0^{+0.4}_{-0.6}$
EMF $\alpha = 1.0$	$9.3^{+1.3}_{-0.8}$	$1.4^{+0.6}_{-0.5}$

Table 2. Time-scales measured using HEISENBERG for observations of the LMC, the averaged PHANGS+NGC300+NGC5194 (PHANGS++ hereafter) observations used as inputs, and for our three simulated galaxies, using gas column density maps for gas with $n > 100 \text{ cm}^{-3}$. Uncertainties for the PHANGS++ observations are the standard deviations of the sample, while uncertainties for the individual galaxies (LMC and simulations) are calculated using the HEISENBERG analysis code. As can be seen, both the cloud lifetimes t_{gas} and feedback timescales t_{FB} for galaxies simulated with EMF are within the observational uncertainties of clouds within the LMC, but shorter than the timescales from the PHANGS++ galaxies.

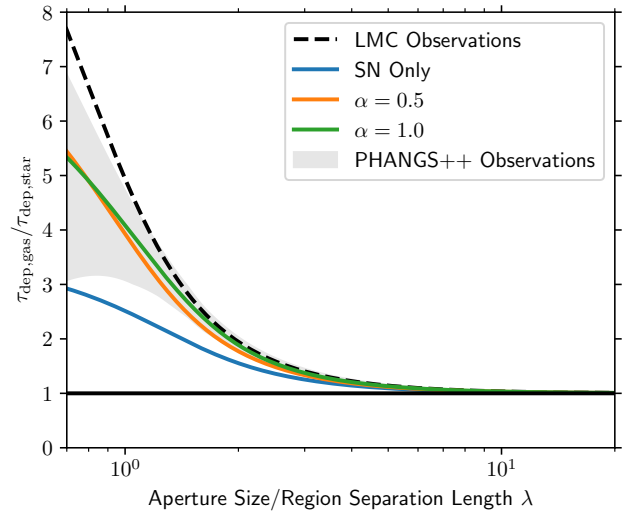


Figure 12. De-correlation ratio of gas and stars at different aperture sizes, for observed galaxies (shaded region and black dashed curve) and our simulations (coloured lines). The de-correlation is measured by the ratio of depletion times measured in apertures centred on dense gas peaks and those measured in apertures centred on young stellar peaks, i.e. the ratio between both branches in Figure 11. As can be seen, the de-correlation measured by $\tau_{\text{dep,gas}}/\tau_{\text{dep,star}}$ for galaxies simulated with EMF lies within the $\pm 1\sigma$ range of observed galaxies, shown by the grey shaded region. With SN feedback only, this ratio is reduced by a factor of ~ 2 , and no longer agrees with the observed range of values.

et al. (2020, 2022). These maps are then stored as FITS files to be read as input by the HEISENBERG code.

In Figure 11, we show the key qualitative metric produced by HEISENBERG, the so-called “tuning fork” diagram that is the fundamental relation defined by the KL14 “uncertainty principle for star formation”. This tuning fork shows the change in gas depletion times $\tau_{\text{dep}} = \Sigma_{\text{gas}}/\Sigma_{\text{SFR}}$ in apertures of various size relative to the globally-averaged depletion time. These apertures are centred on flux peaks identified in the column density maps that we have generated. The upper branch, where we focus apertures on gas peaks, rises above the global average depletion time. The lower arm, where we focus on stellar peaks, dips below the global average depletion time. The width of this opening is determined by the overlap time (t_{FB}), i.e. the duration for which we expect to see spatially-

correlated gas and stellar flux. As t_{FB} goes to zero, the opening widens because cold, dense gas is instantaneously removed from the environment of young stars – observing young stars then implies *not* observing gas, and therefore measuring a short depletion time. As t_{FB} becomes larger, the spread of this opening shrinks and the branches of the tuning fork flatten, because young stars and star-forming gas co-exist for a longer duration of a cloud’s star forming lifetime. The tuning fork will not flatten completely as long as the cloud lifetime is longer than the overlap time-scale ($t_{\text{gas}} > t_{\text{FB}}$) and there exist some clouds without young stars (and vice versa).

In contrast to the feedback time-scale t_{FB} , the ratio of cloud lifetime t_{gas} and young stellar lifetimes control the vertical asymmetry in the tuning fork, and the average region separation length λ controls where the tuning fork begins to open (for more on the information that can be gleaned from the tuning fork diagram, see the detailed description in sect. 3.2.11 of Kruijssen et al. 2018). We normalize our tuning fork diagram by the region separation length λ in order to focus exclusively on the relative width of the opening, which shows the spatial de-correlation of gas and stars and probes the quantities of interest, i.e. the duration of the feedback time-scale t_{FB} and the specific terminal momentum p_0 . In addition to the three simulated galaxies, we also show a tuning fork derived from observations of the Large Magellanic Cloud (LMC; Ward et al. 2020; Kim et al. 2021). We have explicitly not included these measurements in our calculation of the input parameters for EMF, allowing us to use these observations as an independent test of the spatial de-correlation in our simulated galaxies. We select the LMC, because its tuning fork and underlying time-scales provide the best match to those obtained for the simulations analysed here. As can be seen, the de-correlation between gas and stars in the simulation without EMF is too low, resulting in a tuning fork flatter than both the EMF simulations and the observed LMC results.

In Table 2, we show the two primary time-scales derived using HEISENBERG, the gas cloud lifetime t_{gas} and the overlap/feedback time-scale t_{FB} for our simulated galaxies, as well as for the observations of the LMC (Ward et al. 2020; Kim et al. 2021) and the PHANGS++ sample. As these data show, the LMC and our EMF simulated galaxies have comparable cloud lifetimes, approximately within 1σ of each other, with the EMF simulated galaxies having slightly shorter (but mutually indistinguishable) lifetimes of $t_{\text{gas}} \approx 10$ Myr, compared to $t_{\text{gas}} \approx 15$ Myr for galaxies simulated with SN alone. The feedback time-scales are also significantly higher (as we would expect) in the SN-only simulated galaxy, more than 3σ above the feedback time-scale measured in the LMC. By contrast, the feedback time-scales inferred for the simulations with EMF are relatively insensitive to α , with values ranging from 0.5σ higher for $\alpha = 1.0$ to 1.3σ higher for $\alpha = 0.5$.

While the results we find are consistent with a galaxy that was not included among the data we use to derive the parameters p_0 and t_{FB} , we find that the simulated galaxies here do not match the timescales for the observed PHANGS++ galaxies used to derive these parameters. The cloud lifetimes t_{gas} and feedback timescales t_{FB} are both found to be lower in our simulated galaxies that include EMF compared to the median observations of the PHANGS++ sample (though still well within the observed range). In order to determine the sensitivity of these derived values to parameters other than the feedback prescription, we generated gas column density maps with a lower gas cell density threshold (30 cm^{-3}), and re-calculated t_{gas} and t_{FB} . In Appendix C, we also examine the sensitivity to parameter choices for star formation model used. We find we derive significantly ($\sim 4\times$) longer cloud lifetimes, as well as somewhat longer feedback timescales

for all cases when lower-density gas maps are used (as has been seen in the observations of the atomic gas cloud lifetimes seen in Ward et al. 2020).

It should also be noted that while our galaxies simulated with EMF match well the observed feedback timescales in the LMC, there is significant scatter in the PHANGS++ sample, with feedback timescales ranging from 1.0–4.8 Myr. Determining the origin of this scatter, and the potential dependence on environment (see for example Chevance et al. 2022), will require further observational studies. However, in order to fully self-consistently compare measurements of t_{gas} and t_{FB} from simulated galaxies, a full treatment of radiative transfer (RT) and CO chemistry to derive mock CO and $H\alpha$ maps to directly match the observational quantities used to derive these timescales (Fujimoto et al. 2019). While this is beyond the scope of this paper, we are now working on a careful examination of how to most consistently compare RT mock observations of simulated galaxies to true observations (Petkova et al. in prep).

An insightful, alternative quantification of the spatial de-correlation between gas and young stars can be seen in Figure 12. There we show the ratio of the upper branch (centred on dense gas peaks) to the lower branch (centred on young stellar peaks), fitted using HEISENBERG, which we refer to as the de-correlation ratio. This corresponds to the ratio of depletion times measured centred on dense gas versus young stellar peaks, and quantifies the width of the tuning fork in logarithmic space. Importantly, this width is controlled entirely by the feedback time-scale t_{FB} , and the quantity shown in Figure 12 therefore allows us to isolate the contribution of t_{FB} only, without needing to worry about the other dependences on the cloud lifetime and the region separation length. For reference, we also show the $\pm 1\sigma$ range of the de-correlation ratio observed in the PHANGS++ sample of nearby galaxies used to determine the EMF parameters (Kruijssen et al. 2019; Chevance et al. 2020, 2022). As can be seen, the de-correlation ratio for each of our galaxies simulated with EMF lies within the $\pm 1\sigma$ scatter of the observed PHANGS++ galaxies, while the galaxy simulated with SN feedback only lies significantly below this range. This directly reflects the longer feedback time-scale of the SN-only simulation, and clearly demonstrates that EMF is able to reproduce the spatial de-correlation observed in local spiral galaxies, while feedback from SN alone cannot.

5.4 Varying the observationally-derived parameters

In the previous sections, we have examined the effect of varying the observationally unconstrained expansion exponent α , and found that for physically reasonable values ($\alpha = 0.5 - 1.0$), galaxies simulated with EMF show little sensitivity to α . While the two other parameters p_0 and t_{FB} are derived using observational data, there is non-trivial scatter in these observed quantities. Irrespective of whether this is due to environmental variations in the fundamental feedback processes that we parameterise, or simply because of observational uncertainty, it is useful to know how variations in p_0 and t_{FB} change the overall impact of EMF on star formation regulation in our simulated galaxies. In this section, we show how star formation regulation is affected when varying p_0 from 222 km s^{-1} to 452 km s^{-1} and t_{FB} from 2.5 Myr to 4.1 Myr, which corresponds to the interquartile ranges of the observational measurements of these quantities (see Section 3.2). We perform four additional simulations in which we fix $\alpha = 1.0$, while varying p_0 and t_{FB} independently of each other. For runs with modified p_0 ,

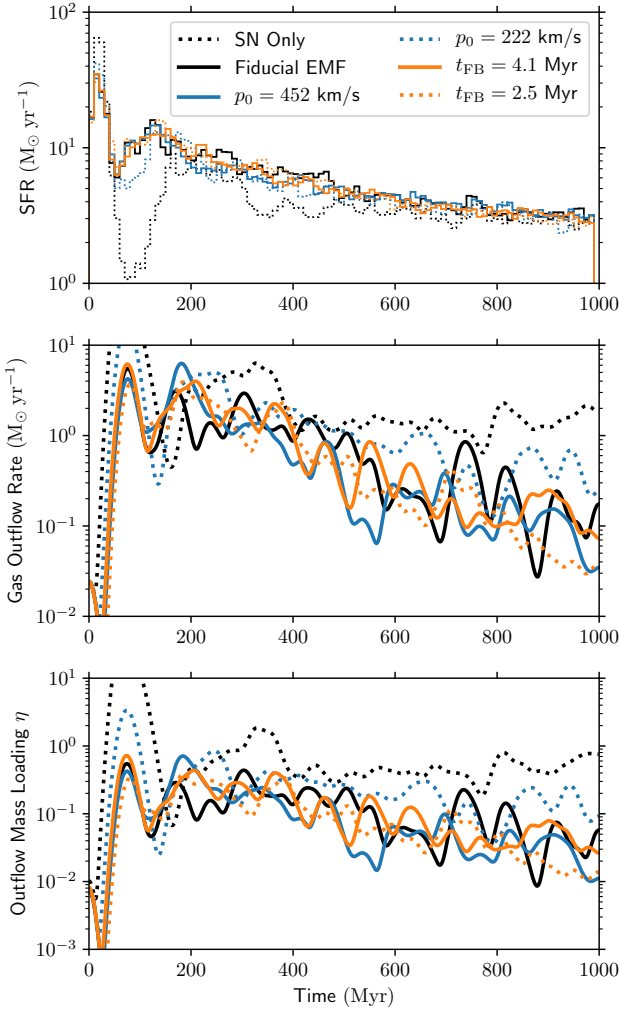


Figure 13. Star formation rates (top panel), outflow rates (middle panel), and mass loadings (bottom panel) for EMF with 25th-to-75th percentile variations in the observationally-derived parameters p_0 (blue curves) and t_{FB} (orange curves). Fiducial parameters are shown in black for the SN-only run (solid) and EMF run with $\alpha = 1.0$ (dotted). As can be seen, varying t_{FB} between 2.5 Myr and 4.1 Myr has little impact on the star formation or outflow rates. However, if p_0 is reduced to 222 km s⁻¹ (from the median observed value of 375 km s⁻¹), we see slightly higher mass loadings and outflow rates, as expected. An analogous shift is not found when increasing p_0 to 452 km s⁻¹, because this does not significantly reduce the overall outflow rates.

we keep t_{FB} fixed at 3.3 Myr, while for modified t_{FB} , we keep p_0 fixed at 375 km s⁻¹.

In Figure 13, we show how the star formation and outflow rates are changed by modifying p_0 and t_{FB} . As we might expect, lowering p_0 pulls the results towards what we see from SN feedback alone (as we are reducing the overall effectiveness of the early stellar feedback). While the SFRs show little difference for any of the cases we examine, the outflow rates and mass loadings do show a small but significant difference. Comparing the outflow rates for the variations in p_0 , the mean outflow rates over the final 500 Myr for $p_0 = \{222, 375, 452\}$ km s⁻¹ are $\{0.58, 0.20, 0.12\}$ M_⊙ yr⁻¹. Changes in t_{FB} do not produce as significant a change compared to p_0 (as we might expect). Adopting $t_{\text{FB}} = \{2.5, 3.3, 4.1\}$ Myr produces mean outflow rates of $\{0.12, 0.20, 0.16\}$ M_⊙ yr⁻¹.

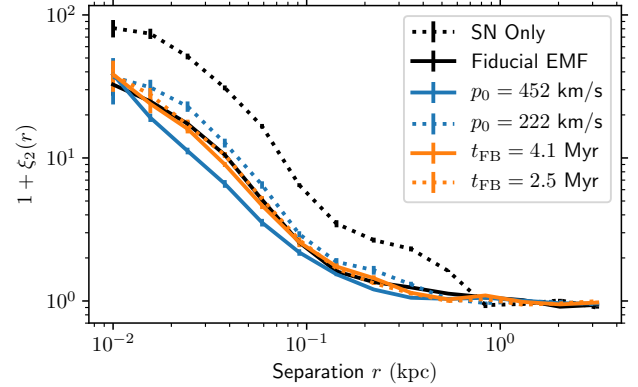


Figure 14. Two-point correlation function of young (< 20 Myr) stars for 25th-to-75th percentile variations in p_0 and t_{FB} . As can be seen, neither increasing nor decreasing t_{FB} produces a change in stellar clustering larger than the uncertainties on ξ_2 . Increasing p_0 produces a slight decrease in clustering on intermediate (30–100 pc) scales, but no detectable difference on the smallest scales (< 20 pc). Decreasing p_0 pushes the results closer to those seen with SN feedback alone, raising the smallest-scale correlation function ξ_2 by a factor of ~ 2 .

As in Figure 7, we can see in Figure 14 that EMF reduces the small-scale (< 1 kpc) clustering of young stars in our simulated disc galaxy. Increasing the value of p_0 slightly decreases the stellar clustering on scales of 20–100 pc, but a much larger increase in the two-point correlation function on small scales is seen when reducing p_0 to 222 km s⁻¹. In turn, this increase in small-scale clustering drives the larger outflow rates and mass loadings we have seen in Figure 13. This weaker form of early feedback produces a result intermediate between EMF with our fiducial parameters and the SN-only example. By contrast, all variations of t_{FB} are within the error bars of each other, and are also consistent with the fiducial parameter choices. We likely would need to vary t_{FB} well beyond the observational constraints to see a significant change in the clustering of young stars or the outflow mass loadings.

6 DISCUSSION

6.1 Previous models for early feedback in galaxy simulations

Early stellar feedback has been studied extensively in simulations of both isolated galaxies and cosmological zoom-in simulations (e.g. Wise & Abel 2008; Stinson et al. 2013; Rosdahl et al. 2015). Many different models have been proposed, and there is still considerable uncertainty as to the quantitative impact of different physical processes and assumptions, as well as different numerical approximations of the same feedback processes.

A number of studies have taken an agnostic approach to the specific driving mechanisms of early stellar feedback, as we have done here. Rather than explicitly modelling individual early stellar feedback processes, these studies use simplifying assumptions about the total stellar feedback budget as the foundation of a model for early stellar feedback. The “MaGICC” early feedback model first presented in Stinson et al. (2013) simply injects 10% of the total stellar luminosity as thermal energy, and has been applied to the large cosmological zoom-in simulations of over 100 galaxies in NIHAO (Wang et al. 2015). Stinson et al. (2013) showed in cosmological zoom-in simulations of an L^* galaxy that this simple

model for early stellar feedback could significantly reduce the overall stellar mass of the galaxy, and help to produce a disc-dominated system with a flat rotation curve. In the recent study by [Semenov et al. \(2021\)](#), stellar winds were approximated by simply shifting the time-scale over which SN detonate to begin 0 Myr after a star particle forms.

A tremendous amount of effort has been spent developing models for early stellar feedback that rely on ionizing radiation. As we detailed in Section 2, ionizing radiation can disrupt star-forming gas through direct and indirect radiation pressure, photoionization, and by the expansion of overpressured HII regions ([Kim et al. 2018](#)). Studies looking at early radiative feedback have typically used one of two approaches: capturing radiative feedback through explicit radiative transfer, or by approximating each mechanism of radiative feedback with sub-resolution models. Explicit radiative transfer tends to be numerically expensive, and so approximations are required to achieve reasonable performance in both the scaling of the algorithm with source and particle number as well as the timestep required for numerical stability. Early studies employing ray-tracing techniques (e.g. [Wise & Abel 2008](#)) were limited to studying extremely high-redshift objects, while others looked at smaller, dwarf-scale objects (e.g. [Kim et al. 2013](#)). The development of tree-based radiative transfer algorithms ([Kannan et al. 2014](#); [Obreja et al. 2019](#); [Benincasa et al. 2020](#)) may allow much larger-scale radiative transfer simulations in the future. Even when the full radiative transfer equations (including scattering and re-emission) are followed, limited resolution in the highest density regions of the ISM may still require significant sub-grid approximations ([Rosdahl et al. 2015](#)). This has been a particular focus for studies of reionization, as the escape fraction of ionizing photons depends strongly on the fractal, porous structure of unresolved GMCs ([Kimm & Cen 2014](#); [Ma et al. 2015](#); [Trebitsch et al. 2017](#)).

Sidestepping the additional cost of full radiative transfer has generally relied on the assumption that most of the impact of radiative feedback is local, concentrated in the immediate vicinity of a star-forming region. Local radiative models have been built to capture the effects of HII region expansion ([Jeffreson et al. 2021b](#)), radiation pressure ([Roškar et al. 2014](#); [Ceverino et al. 2014](#)), and photoionization ([Smith et al. 2021](#)). In general, these models find that radiative feedback is sub-dominant to SN feedback in most galactic environments ([Su et al. 2017](#)), but may act to either boost ([Hopkins et al. 2011](#)) or suppress ([Smith et al. 2021](#)) SN-driven galactic outflows. Further research is required to fully understand the interplay of radiative early feedback, SN driven outflows, and galaxy-scale regulation.

An exciting new field of study for the comprehensive effects of early stellar feedback is in ultra-high resolution simulations of isolated dwarf galaxies, where the internal structure of star-forming GMCs becomes resolvable ([Emerick et al. 2019](#); [Hu et al. 2017](#); [Smith et al. 2021](#)). Both [Hu et al. \(2017\)](#) and [Smith et al. \(2021\)](#) find similar effects in these well-resolved simulations when photoelectric heating and photoionization are included on top of SN feedback alone. They find increased outflow rates and a significantly more disrupted ISM structures when early feedback is omitted. This agrees qualitatively with the results we show here, even though their simulations have mass resolutions ~ 1000 times better than the galaxies we have simulated (note that their simulated galaxies are also roughly a factor of ~ 100 less massive than the L^* objects we simulate here). With baryonic mass resolutions of $\ll 100 M_\odot$, not only is the internal structure of GMCs accessible, but simulations become capable of tracking individual massive stars, forming physically-resolved (although not dynamically-resolved) star clus-

ters and resolving the complex interplay between feedback fronts driven by each massive star. These simulations offer a new frontier to understand how feedback disrupts these clouds in a realistic galactic environment. Unfortunately, these extreme resolutions are well out of reach for simulations of more massive galaxies, especially those that include a full cosmological environment. Despite this, they are an excellent tool for understanding how the observational momentum inputs and time-scales arise, and what feedback mechanisms dominate this momentum budget.

In addition to detailed studies looking at individual early feedback processes, there is an abundance of studies that attempt to include complete accountings of the stellar feedback budget, including both winds and radiative processes (e.g. [Trujillo-Gomez et al. 2015](#); [Goldbaum et al. 2016](#); [Marinacci et al. 2019](#)). [Agertz et al. \(2013\)](#) presented a detailed budgeting of the momentum and energy injection from massive stars, and developed a model that has been used to study the cosmological evolution of galaxies ([Agertz & Kravtsov 2015](#)). The FIRE ([Hopkins et al. 2014](#)) and FIRE-2 ([Hopkins et al. 2018b](#)) have been used for numerous studies using cosmological zoom-in simulations of galaxies with virial masses ranging from $\sim 10^9 M_\odot$ to $\sim 10^{12} M_\odot$. FIRE includes explicit sub-grid models for early feedback from stellar winds, radiation pressure, and photoionization. These early feedback mechanisms were shown in [Hopkins et al. \(2014\)](#) to enhance the efficiency of SN at regulating the stellar and baryonic mass of galaxies, though there remains some uncertainty as to the magnitude of the effect in light of the approximate nature of the sub-grid models used.

Physically-motivated models for individual feedback mechanisms will be a fruitful comparison tool to the EMF model we have presented here. While EMF is designed to match observed cloud-scale feedback timescales, we have taken an agnostic approach as to which particular feedback mechanism is dominant, whether any single mechanism can explain these observed timescales, and if this depends on galactic environment. By comparing different physical mechanisms of early stellar feedback to both observations and simulations using EMF, we can better understand the underlying physics that drives the disruption of GMCs in the diverse galactic environments they find themselves in.

6.2 Spatial de-correlation and tuning forks in previous simulations

Since the introduction of the “tuning fork diagram” by [Schruba et al. \(2010\)](#), its analytical characterisation in terms of time-scales by [KL14](#), and the initial suite of galaxy simulations demonstrating its suitability for accurately characterising the cloud lifecycle ([Kruijssen et al. 2018](#)), five further simulation studies have used this technique to examine the lifetimes of molecular clouds and the cloud-scale feedback cycle. While these studies did not attempt to build feedback models directly from observational measurements of cloud life cycles, they did use the tuning fork diagram as a diagnostic for characterising stellar feedback processes.

The first of these studies, [Fujimoto et al. \(2019\)](#), used AMR simulations of an isolated, Milky Way-like galaxy similar to what we have examined here, but with higher resolution refinement to a minimum cell size of ~ 7 pc in the Eulerian hydrodynamic code ENZO ([Bryan et al. 2014](#)). Their star formation algorithm is the same as what we use here, and they include stellar feedback from SNe and photoionization from young massive stars. Their photoionization early feedback model calculates the Strömgren volume from the luminosity of stars, and then heats an appropriate region to 10^4 K. For SNe feedback, their simulations directly inject the

terminal momentum ($5 \times 10^5 \text{ M}_\odot \text{ km s}^{-1}$) into the cells surrounding each SN event, and deposit the remaining thermal energy in the SN host cell. The [Kimm & Cen \(2014\)](#) mechanical feedback model that we apply deposits comparable momentum in the limit of infinitely poor resolution, but additionally adaptively scales the ratio of kinetic to thermal energy injected based on the local resolution. Unlike our study, [Fujimoto et al. \(2019\)](#) use the DESPOTIC ([Krumholz 2014](#)) radiative transfer code to post-process their simulations, in order to generate CO $J = 1 \rightarrow 0$, HI, and H α emission maps. They find that the feedback model in their simulations produced long-lived clouds, with average lifetimes of 36^{+4}_{-6} Myr and extremely long feedback time-scales of 23 ± 1 Myr, measured using the KL14 methodology. [Fujimoto et al. \(2019\)](#) attributes these long lifetimes to ineffective photoionization feedback. These simulations seem to regulate star formation through slow and (very) inefficient star formation, rather than the fast and inefficient mode seen in our simulations and in the observations of [Kruijssen et al. \(2019\)](#), [Chevance et al. \(2020, 2022\)](#), and [Kim et al. \(2021\)](#).

Another recent trilogy of papers ([Jeffreson et al. 2020, 2021a,b](#)) have examined tuning fork diagrams in simulated Milky Way-like galaxies. These simulations use an identical model for SNe feedback as we have employed here (in fact, the same implementation in the AREPO numerical code), but also include a model for momentum injection via unresolved HII regions described in [Jeffreson et al. \(2021b\)](#). [Jeffreson et al. \(2021b\)](#) finds that the small-scale spatial de-correlation of gas and stars is impacted somewhat less significantly by early feedback from HII regions, reducing t_{FB} from > 5 Myr to 4.4 Myr. In [Jeffreson et al. \(2021a\)](#), the authors use high-resolution simulations of a Milky Way like galaxy, along with the ASTRODENDRO ([Robitaille et al. 2019](#)) cloud-finding tool to trace individual molecular clouds and quantify their evolution over time. They find that in these galaxies, the opening of the tuning fork on small scales gives de-correlation ratios $\tau_{\text{dep,gas}}/\tau_{\text{dep,star}} \sim 4$, within the range of the PHANGS observations, although somewhat lower than the values of ~ 5.5 we find here. The authors then use these same simulations to derive new scaling relations for cloud lifetimes in Milky Way-like galaxies. They find the average time-scales derived from directly tracking clouds from high-cadence simulations (1 Myr temporal resolution) is generally in agreement with the averaged cloud lifetimes derived using the methodology of [Kruijssen et al. \(2018\)](#).

More recently, a comprehensive study by [Semenov et al. \(2021\)](#) has looked at the combined effects of explicitly modelled radiative transfer, H₂ chemistry, unresolved turbulent pressure, early mechanical feedback, and a turbulence-based star formation model. They model early feedback through UV photoheating and photoionization, along with a simple model for early mechanical feedback that simply shifts the injection of SN energy to begin immediately after the first star forms (a discussion of the impact of SN injection timings can be found in [Keller & Kruijssen 2022](#)). Unresolved turbulence is captured using a model first presented by [Semenov et al. \(2016\)](#), which accounts for the turbulent energy cascade below the resolution scale of the simulations. [Semenov et al. \(2021\)](#) examine a number of star formation models, including a simple Schmidt law similar to what we have used here, a Schmidt law with a virial parameter cutoff mimicking the FIRE-2 star formation model ([Hopkins et al. 2018b](#)), and a model based on the [Padoan et al. \(2012\)](#) small-scale simulations of star formation (a similar model was also recently described in [Gensior et al. 2020](#)). They use initial conditions of an isolated disc galaxy with general properties designed to match NGC300, allowing them to compare to the observations presented by [Kruijssen et al. \(2019\)](#). With

an array of simulations using different selections of feedback processes and star formation parameter choices, they demonstrate how strong early feedback increases the de-correlation ratio, as we have demonstrated here for the EMF model. For very high star formation efficiencies with a Schmidt-type star formation law, they in fact find de-correlation ratios much higher than NGC300. In their simulations with SN feedback alone, they also find that the de-correlation ratio is much smaller than the observational values (as indicated by a smaller opening of the tuning fork on small scales), consistently with our results. Interestingly, they also show that self-consistent radiative early feedback is important for setting the region separation length λ .

6.3 Limitations and future directions

The EMF model we present here relies primarily on the observational constraints on p_0 and t_{FB} . Currently, we have used a sample only 10 nearby disc galaxies to obtain these quantities. Future observations of a larger galaxy sample (J. Kim et al. in prep.) will provide us with the statistics needed to improve our understanding of how these parameters change in different environments. This will be aided further by additionally extending the sample to more extreme environments, such as metal-poor dwarf galaxies, gas-rich starbursts, and massive ellipticals. Of particular interest will be to derive scaling relations between p_0 , t_{FB} , and the galactic environment (e.g. local ISM properties). Further, more detailed studies of the relationship between the ISM and feedback timescales in observed galaxies will allow us to develop an improved, environmentally-dependent version of EMF that will more accurately model the effects of early feedback in galaxies very different than the isolated L^* discs at $z = 0$ that we have studied here.

Of particular interest and challenge is the pressure (and thus) scale height of the ISM. As we derive our model using self-similar, spherical wind models, a feedback bubble will diverge from the simple equation 3 when the ISM pressure becomes comparable to the ram pressure of the feedback front, and when the radius of the bubble becomes comparable to the ISM scale height ([Mac Low & McCray 1988](#)). Treating the non-spherical evolution of non-self-similar feedback fronts is a particularly challenging problem for sub-grid models for feedback, especially if one wishes to build models with reasonable convergence properties. In particular, bridging the resolution gap from low-resolution simulations that do not resolve the ISM scale height (as is the current state of the art in large cosmological volumes) to higher resolution simulations of galaxies with a well-resolved ISM may not be possible with a single model for feedback.

Environmentally-dependent EMF will be of particular importance for cosmological simulations, as even galaxies that are similar to the isolated discs we study here at $z = 0$ will spend much of their lifetime as considerably smaller, more metal-poor progenitors in a more merger-rich environment. EMF is well-suited for cosmological simulations, as it is numerically inexpensive, and shows good convergence properties (see Appendix A). Future observations will help reveal how generalizable the current values for p_0 and t_{FB} are for both the progenitors of L^* galaxies as well as for a wide variety of galaxy masses observed at $z = 0$.

We have demonstrated that EMF can reproduce the observed spatial de-correlation of gas and stars, and presented a method for deriving the terminal momentum injected by early feedback from this observed de-correlation. However, this model is incapable of investigating the ultimate cause of the observed short feedback

time-scales, as well as how the small-scale interaction of multiple feedback processes produce the momentum inferred from observational data. The values of p_0 and t_{FB} are assumed as input parameters to our model, and are agnostic to the underlying physics that set these quantities. High resolution simulations that resolve individual massive stars and the GMCs in which they are born are the most effective way forward to answer this question, whether that be simulations of individual GMCs (e.g. [Geen et al. 2018](#)), stratified slices of the ISM (e.g. [Gatto et al. 2017](#)), or isolated dwarf galaxies (e.g. [Smith et al. 2021](#)).

7 CONCLUSIONS

We have presented here a new numerical model for early stellar feedback that for the first time uses parameters directly constrained through observational measurements. Using the self-similar evolution of feedback fronts, we apply measurements of the feedback timescale t_{FB} , cloud radius r_{cl} , and star formation efficiency ϵ_{SF} to derive the empirically-motivated terminal momentum p_0 . Our model captures uncertainty in the cloud-scale star formation rate and the true driving mechanism through a single dimensionless quantity, the expansion exponent α . As we have shown, not only is this parameter physically constrained to a narrow range, $\sim 0.5 - 1$, and galaxies simulated using empirically-motivated early stellar feedback are also relatively insensitive to the value of the expansion exponent.

Using a suite of simulated Milky Way-like galaxies, we have examined how observationally-constrained early stellar feedback drives both quantitative and qualitative changes in the overall evolution of these simulated galaxies. We find that the overall regulation of the star formation rate is only marginally affected by the inclusion of EMF. After an initial period of settling, galaxies simulated with EMF show a slightly higher ($\sim 10 - 15\%$) star formation rate, and a slightly steeper Kennicutt-Schmidt relation, than those simulated with SN feedback alone. While an increase in star formation due to additional feedback may seem surprising at first, we find that this occurs due to a fundamental change in the spatio-temporal distribution of star formation. Without the early disruption of star forming clouds provided by EMF, we see a significant, quantitative increase in star particles forming co-spatially. This in turn results in a marked change in how SNe couple to the surrounding ISM. Without EMF, overlapping SNe blastwaves generate more hot, diffuse gas within the ISM, losing less of their energy to radiative losses. Qualitatively, this produces an ISM with large voids, as seen in column density maps when EMF is omitted. Quantitatively, the reduction of hot, SN-heated gas we see with EMF results in a ~ 1 dex decrease in outflow mass loadings, and produces thinner gaseous and discs. This suggests that EMF may be a solution to the difficulty recent simulation studies ([Roškar et al. 2014](#); [Grand et al. 2017](#)) have found in producing truly thin discs, though this will require fully cosmological simulations to fully explore. The significant changes in the SN-driven outflow behaviour that EMF produces also has significant implications for future observational surveys of outflow launching and the resolved mass and metal content of the CGM.

In future work, we will apply this model to cosmological simulations of galaxies, and incorporate improved measurements of the observationally-derived parameters constraining the total momentum budget (p_0) and time-scale (t_{FB}), including their dependence on the galactic environment. With this, we will be able to disentangle the effects of early feedback and the cosmological assembly

of galaxies in realistic environments, and examine how the effects we have measured in isolated, Milky Way-like galaxies produce changes across the cosmic lifetime of simulated galaxies.

ACKNOWLEDGEMENTS

We thank Volker Springel for giving us access to AREPO. We thank Sam Geen, Jindra Gensior, Sarah Jeffreson, Steve Longmore, and Lachlan Lancaster for valuable conversations regarding this paper. BWK, JMDK, and MC gratefully acknowledge funding from the European Research Council (ERC) under the European Union’s Horizon 2020 research and innovation programme via the ERC Starting Grant MUSTANG (grant agreement number 714907). BWK acknowledges funding in the form of a Postdoctoral Research Fellowship from the Alexander von Humboldt Stiftung. JMDK and MC gratefully acknowledge funding from the German Research Foundation (DFG) in the form of an Emmy Noether Research Group (grant number KR4801/1-1) and the DFG Sachbeihilfe (grant number KR4801/2-1).

DATA AVAILABILITY STATEMENT

The simulation data used in this paper will be shared on reasonable request to the corresponding author.

REFERENCES

- Agertz O., Kravtsov A. V., 2015, [ApJ](#), **804**, 18
- Agertz O., Kravtsov A. V., Leitner S. N., Gnedin N. Y., 2013, [ApJ](#), **770**, 25
- Benincasa S. M., Wadsley J., Couchman H. M. P., Keller B. W., 2016, [MNRAS](#), **462**, 3053
- Benincasa S. M., Wadsley J. W., Couchman H. M. P., Pettitt A. R., Keller B. W., Woods R. M., Grond J. J., 2020, [MNRAS](#), **499**, 2028
- Bigiel F., Leroy A., Walter F., Brinks E., de Blok W. J. G., Madore B., Thornley M. D., 2008, [AJ](#), **136**, 2846
- Bigiel F., et al., 2011, [ApJ](#), **730**, L13
- Blondin J. M., Wright E. B., Borkowski K. J., Reynolds S. P., 1998, [ApJ](#), **500**, 342
- Bryan G. L., et al., 2014, [ApJS](#), **211**, 19
- Bullock J. S., Dekel A., Kolatt T. S., Kravtsov A. V., Klypin A. A., Porciani C., Primack J. R., 2001, [ApJ](#), **555**, 240
- Calzetti D., et al., 2015, [AJ](#), **149**, 51
- Ceverino D., Klypin A., Klimek E. S., Trujillo-Gomez S., Churchill C. W., Primack J., Dekel A., 2014, [MNRAS](#), **442**, 1545
- Chabrier G., 2003, [PASP](#), **115**, 763
- Chevance M., et al., 2020, [MNRAS](#), **493**, 2872
- Chevance M., et al., 2022, [MNRAS](#), **509**, 272
- Christensen C., Quinn T., Governato F., Stilp A., Shen S., Wadsley J., 2012, [MNRAS](#), **425**, 3058
- Cioffi D. F., McKee C. F., Bertschinger E., 1988, [ApJ](#), **334**, 252
- Costa T., Rosdahl J., Sijacki D., Haehnelt M. G., 2018, [MNRAS](#), **473**, 4197
- Dale J. E., 2017, [MNRAS](#), **467**, 1067
- Dale J. E., Bonnell I. A., Clarke C. J., Bate M. R., 2005, [MNRAS](#), **358**, 291
- Dale J. E., Ngoumou J., Ercolano B., Bonnell I. A., 2014, [MNRAS](#), **442**, 694
- Ekström S., et al., 2012, [A&A](#), **537**, A146
- Eldridge J. J., Izzard R. G., Tout C. A., 2008, [MNRAS](#), **384**, 1109
- Emerick A., Bryan G. L., Mac Low M.-M., 2019, [MNRAS](#), **482**, 1304
- Evans Neal J. I., et al., 2009, [ApJS](#), **181**, 321
- Ferland G. J., et al., 2013, [RMxAA](#), **49**, 137
- Fielding D., Quataert E., Martizzi D., 2018, [MNRAS](#), **481**, 3325
- Fielding D. B., Ostriker E. C., Bryan G. L., Jermyn A. S., 2020, [ApJ](#), **894**, L24

- Fierlinger K. M., Burkert A., Ntormousi E., Fierlinger P., Schartmann M., Ballone A., Krause M. G. H., Diehl R., 2016, *MNRAS*, **456**, 710
- Font A. S., et al., 2020, *MNRAS*, **498**, 1765
- Franco J., Tenorio-Tagle G., Bodenheimer P., 1990, *ApJ*, **349**, 126
- Fujimoto Y., Chevance M., Haydon D. T., Krumholz M. R., Kruijssen J. M. D., 2019, *MNRAS*, **487**, 1717
- Gatto A., et al., 2017, *MNRAS*, **466**, 1903
- Geen S., Rosdahl J., Blaizot J., Devriendt J., Slyz A., 2015, *MNRAS*, **448**, 3248
- Geen S., Watson S. K., Rosdahl J., Bieri R., Klessen R. S., Hennebelle P., 2018, *MNRAS*, **481**, 2548
- Geen S., Bieri R., Rosdahl J., de Koter A., 2021, *MNRAS*, **501**, 1352
- Genel S., et al., 2019, *ApJ*, **871**, 21
- Gensior J., Kruijssen J. M. D., Keller B. W., 2020, *MNRAS*, **495**, 199
- Gentry E. S., Madau P., Krumholz M. R., 2020, *MNRAS*, **492**, 1243
- Goldbaum N. J., Krumholz M. R., Forbes J. C., 2016, *ApJ*, **827**, 28
- Grand R. J. J., et al., 2017, *MNRAS*, **467**, 179
- Grisdale K., Agertz O., Renaud F., Romeo A. B., Devriendt J., Slyz A., 2019, *MNRAS*, **486**, 5482
- Grudić M. Y., Hopkins P. F., Lee E. J., Murray N., Faucher-Giguère C.-A., Johnson L. C., 2019, *MNRAS*, **488**, 1501
- Grudić M. Y., Guszejnov D., Hopkins P. F., Offner S. S. R., Faucher-Giguère C.-A., 2021, *MNRAS*, **506**, 2199
- Guedes J., Callegari S., Madau P., Mayer L., 2011, *ApJ*, **742**, 76
- Haardt F., Madau P., 2012, *ApJ*, **746**, 125
- Haid S., Walch S., Seifried D., Wünsch R., Dinnbier F., Naab T., 2019, *MNRAS*, **482**, 4062
- Helmi A., Babusiaux C., Koppelman H. H., Massari D., Veljanoski J., Brown A. G. A., 2018, *Nature*, **563**, 85
- Heyer M., Gutermuth R., Urquhart J. S., Csengeri T., Wienen M., Leurini S., Menten K., Wyrowski F., 2016, *A&A*, **588**, A29
- Hopkins P. F., Quataert E., Murray N., 2011, *MNRAS*, **417**, 950
- Hopkins P. F., Kereš D., Oñorbe J., Faucher-Giguère C.-A., Quataert E., Murray N., Bullock J. S., 2014, *MNRAS*, **445**, 581
- Hopkins P. F., et al., 2018a, *MNRAS*, **477**, 1578
- Hopkins P. F., et al., 2018b, *MNRAS*, **480**, 800
- Hu C.-Y., Naab T., Glover S. C. O., Walch S., Clark P. C., 2017, *MNRAS*, **471**, 2151
- Jeffreson S. M. R., Kruijssen J. M. D., Keller B. W., Chevance M., Glover S. C. O., 2020, *MNRAS*, **498**, 385
- Jeffreson S. M. R., Keller B. W., Winter A. J., Chevance M., Kruijssen J. M. D., Krumholz M. R., Fujimoto Y., 2021a, *MNRAS*, **501**, 1352
- Jeffreson S. M. R., Krumholz M. R., Fujimoto Y., Armillotta L., Keller B. W., Chevance M., Kruijssen J. M. D., 2021b, *MNRAS*, **505**, 3470
- Joung M. K. R., Mac Low M.-M., 2006, *ApJ*, **653**, 1266
- Kahn F. D., 1954, *Bull. Astron. Inst. Netherlands*, **12**, 187
- Kannan R., et al., 2014, *MNRAS*, **437**, 2882
- Keller B. W., Kruijssen J. M. D., 2022, *MNRAS*, **512**, 199
- Keller B. W., Wadsley J., Benincasa S. M., Couchman H. M. P., 2014, *MNRAS*, **442**, 3013
- Keller B. W., Wadsley J., Couchman H. M. P., 2015, *MNRAS*, **453**, 3499
- Keller B. W., Wadsley J. W., Wang L., Kruijssen J. M. D., 2019, *MNRAS*, **482**, 2244
- Kennicutt Jr. R. C., 1998, *ARAA*, **36**, 189
- Kim J.-h., Krumholz M. R., Wise J. H., Turk M. J., Goldbaum N. J., Abel T., 2013, *ApJ*, **775**, 109
- Kim J.-h., et al., 2014, *ApJS*, **210**, 14
- Kim J.-G., Kim W.-T., Ostriker E. C., 2018, *ApJ*, **859**, 68
- Kim J., et al., 2021, *MNRAS*, **504**, 487
- Kimm T., Cen R., 2014, *ApJ*, **788**, 121
- Körtgen B., Seifried D., Banerjee R., Vázquez-Semadeni E., Zamora-Avilés M., 2016, *MNRAS*, **459**, 3460
- Kroupa P., 2001, *MNRAS*, **322**, 231
- Kroupa P., Weidner C., 2003, *ApJ*, **598**, 1076
- Kruijssen J. M. D., Longmore S. N., 2014, *MNRAS*, **439**, 3239
- Kruijssen J. M. D., Schrubba A., Hygate A. P. S., Hu C.-Y., Haydon D. T., Longmore S. N., 2018, *MNRAS*, **479**, 1866
- Kruijssen J. M. D., et al., 2019, *Nature*, **569**, 519
- Kruijssen J. M. D., et al., 2020, *MNRAS*, **498**, 2472
- Krumholz M. R., 2014, *MNRAS*, **437**, 1662
- Krumholz M. R., Matzner C. D., 2009, *ApJ*, **703**, 1352
- Krumholz M. R., Thompson T. A., 2012, *ApJ*, **760**, 155
- Krumholz M. R., Fumagalli M., da Silva R. L., Rendahl T., Parra J., 2015, *MNRAS*, **452**, 1447
- Lancaster L., Ostriker E. C., Kim J.-G., Kim C.-G., 2021a, *ApJ*, **914**, 89
- Lancaster L., Ostriker E. C., Kim J.-G., Kim C.-G., 2021b, *ApJ*, **914**, 90
- Landy S. D., Szalay A. S., 1993, *ApJ*, **412**, 64
- Larson R. B., 1974, *MNRAS*, **169**, 229
- Larson R. B., 1981, *MNRAS*, **194**, 809
- Lee J. C., et al., 2022, *ApJS*, **258**, 10
- Leitherer C., Robert C., Drissen L., 1992, *ApJ*, **401**, 596
- Leitherer C., Ekström S., Meynet G., Schaerer D., Agienko K. B., Levesque E. M., 2014, *ApJS*, **212**, 14
- Leroy A. K., Walter F., Brinks E., Bigiel F., de Blok W. J. G., Madore B., Thornley M. D., 2008, *AJ*, **136**, 2782
- Leroy A. K., et al., 2021, *ApJS*, **257**, 43
- Lynds C. R., Sandage A. R., 1963, *ApJ*, **137**, 1005
- Ma X., Kasen D., Hopkins P. F., Faucher-Giguère C.-A., Quataert E., Kereš D., Murray N., 2015, *MNRAS*, **453**, 960
- Mac Low M.-M., McCray R., 1988, *ApJ*, **324**, 776
- Maeder A., Meynet G., 1989, *A&A*, **210**, 155
- Maoz D., Mannucci F., Brandt T. D., 2012, *MNRAS*, **426**, 3282
- Marinacci F., Sales L. V., Vogelsberger M., Torrey P., Springel V., 2019, *MNRAS*, **489**, 4233
- Martizzi D., 2020, *MNRAS*, **492**, 79
- McKee C. F., Ostriker J. P., 1977, *ApJ*, **218**, 148
- Mokiem M. R., et al., 2007, *A&A*, **473**, 603
- Murray N., Quataert E., Thompson T. A., 2010, *ApJ*, **709**, 191
- Naidu R. P., et al., 2021, *ApJ*, **923**, 92
- Nelson D., et al., 2019, *MNRAS*, **490**, 3234
- Obreja A., Macciò A. V., Moster B., Udrescu S. M., Buck T., Kannan R., Dutton A. A., Blank M., 2019, *MNRAS*, **490**, 1518
- Ostriker J. P., McKee C. F., 1988, *Reviews of Modern Physics*, **60**, 1
- Padoan P., Haugbølle T., Nordlund Å., 2012, *ApJ*, **759**, L27
- Raskutti S., Ostriker E. C., Skinner M. A., 2016, *ApJ*, **829**, 130
- Reina-Campos M., Kruijssen J. M. D., 2017, *MNRAS*, **469**, 1282
- Robitaille T., Rice T., Beaumont C., Ginsburg A., MacDonald B., Rosolowsky E., 2019, *astrodendro: Astronomical data dendrogram creator (ascl:1907.016)*
- Rogers H., Pittard J. M., 2013, *MNRAS*, **431**, 1337
- Rosdahl J., Schaye J., Teyssier R., Agertz O., 2015, *MNRAS*, **451**, 34
- Rosdahl J., Schaye J., Dubois Y., Kimm T., Teyssier R., 2017, *MNRAS*, **466**, 11
- Rousseau-Nepton L., et al., 2019, *MNRAS*, **489**, 5530
- Roškar R., Teyssier R., Agertz O., Wetzstein M., Moore B., 2014, *MNRAS*, **444**, 2837
- Sawala T., et al., 2016, *MNRAS*, **457**, 1931
- Scannapieco C., et al., 2012, *MNRAS*, **423**, 1726
- Schinnerer E., et al., 2013, *ApJ*, **779**, 42
- Schruba A., Leroy A. K., Walter F., Sandstrom K., Rosolowsky E., 2010, *ApJ*, **722**, 1699
- Seitenzahl I. R., et al., 2013, *MNRAS*, **429**, 1156
- Semenov V. A., Kravtsov A. V., Gnedin N. Y., 2016, *ApJ*, **826**, 200
- Semenov V. A., Kravtsov A. V., Gnedin N. Y., 2021, *ApJ*, **918**, 13
- Simpson C. M., Pakmor R., Marinacci F., Pfrommer C., Springel V., Glover S. C. O., Clark P. C., Smith R. J., 2016, *ApJ*, **827**, L29
- Smith B. D., et al., 2017, *MNRAS*, **466**, 2217
- Smith M. C., Sijacki D., Shen S., 2018, *MNRAS*, **478**, 302
- Smith M. C., Bryan G. L., Somerville R. S., Hu C.-Y., Teyssier R., Burkhardt B., Hernquist L., 2021, *MNRAS*, **506**, 3882
- Somerville R. S., Primack J. R., 1999, *MNRAS*, **310**, 1087
- Spitzer Jr. L., 1956, *ApJ*, **124**, 20
- Spitzer L., 1978, *Physical processes in the interstellar medium*, doi:10.1002/9783527617722.
- Springel V., 2010, *MNRAS*, **401**, 791
- Springel V., Di Matteo T., Hernquist L., 2005, *MNRAS*, **361**, 776

- Stinson G. S., Brook C., Macciò A. V., Wadsley J., Quinn T. R., Couchman H. M. P., 2013, *MNRAS*, **428**, 129
- Strömgren B., 1939, *ApJ*, **89**, 526
- Su K.-Y., Hopkins P. F., Hayward C. C., Faucher-Giguère C.-A., Kereš D., Ma X., Robles V. H., 2017, *MNRAS*, **471**, 144
- Sukhbold T., Ertl T., Woosley S. E., Brown J. M., Janka H. T., 2016, *ApJ*, **821**, 38
- Trebtsch M., Blaizot J., Rosdahl J., Devriendt J., Slyz A., 2017, *MNRAS*, **470**, 224
- Tremmel M., Karcher M., Governato F., Volonteri M., Quinn T. R., Pontzen A., Anderson L., Bellovary J., 2017, *MNRAS*, **470**, 1121
- Truelove J. K., Klein R. I., McKee C. F., Holliman John H. I., Howell L. H., Greenough J. A., 1997, *ApJ*, **489**, L179
- Trujillo-Gomez S., Klypin A., Colín P., Ceverino D., Arraki K. S., Primack J., 2015, *MNRAS*, **446**, 1140
- Vogelsberger M., et al., 2014, *MNRAS*, **444**, 1518
- Walch S. K., Whitworth A. P., Bisbas T., Wünsch R., Hubber D., 2012, *MNRAS*, **427**, 625
- Wang L., Dutton A. A., Stinson G. S., Macciò A. V., Penzo C., Kang X., Keller B. W., Wadsley J., 2015, *MNRAS*, **454**, 83
- Ward J. L., Chevance M., Kruijssen J. M. D., Hygate A. P. S., Schruha A., Longmore S. N., 2020, *MNRAS*, **497**, 2286
- Wareing C. J., Pittard J. M., Falle S. A. E. G., 2017, *MNRAS*, **465**, 2757
- Weaver R., McCray R., Castor J., Shapiro P., Moore R., 1977, *ApJ*, **218**, 377
- Wise J. H., Abel T., 2008, *ApJ*, **685**, 40
- Yu S., et al., 2020, *MNRAS*, **494**, 1539
- Zabel N., et al., 2020, *MNRAS*, **496**, 2155

APPENDIX A: CONVERGENCE PROPERTIES

The EMF model has been designed specifically for use in simulations that do not resolve the detailed interior structure of molecular clouds and the interaction of early feedback processes within these clouds. The fiducial resolution used in the isolated galaxy simulations we have presented here ($M_{\text{gas}} = 8.6 \times 10^3 M_{\odot}$) is comparable to existing high-resolution cosmological zoom-in galaxy simulations (Guedes et al. 2011; Sawala et al. 2016; Hopkins et al. 2018b; Font et al. 2020), but is significantly higher than is achievable in large-volume cosmological simulations (Tremmel et al. 2017; Nelson et al. 2019). In order to ensure the impact of our new models converge at the lower resolution required for cosmological (rather than isolated) simulations, we have re-run the simulation using EMF with the median parameters $p_0 = 377 \text{ km s}^{-1}$, $t_{\text{FB}} = 3.3 \text{ Myr}$, and with $\alpha = 1.0$ at a degraded resolution. The degraded simulation has the same global disc properties as the fiducial resolution, but with all particle masses increased by a factor of 10, such that the degraded DM mass resolution is $1.254 \times 10^7 M_{\odot}$, while the baryonic mass resolution is $8.6 \times 10^4 M_{\odot}$. We also increase the softening by a factor of two (to 80 pc), and decrease the minimum density threshold for star formation to 1 cm^{-3} to account for the reduced ability to resolve dense gas at the degraded resolution.

The SFR and outflow rates for this test are shown in Figure A1. As can be seen from this Figure, the star formation rate and outflow rates are reasonably converged, with some stochastic variation between the fiducial and degraded resolution, especially for the duration of their re-equilibration after the start of the simulation (the first $\sim 600 \text{ Myr}$). Both resolutions show the same difference compared to the SN-only run, with roughly comparable star formation rates, but outflow rates lower by ~ 1 dex.

We see a similar weak dependence on resolution for the gas temperature and density distributions shown in Figure A2. Again,

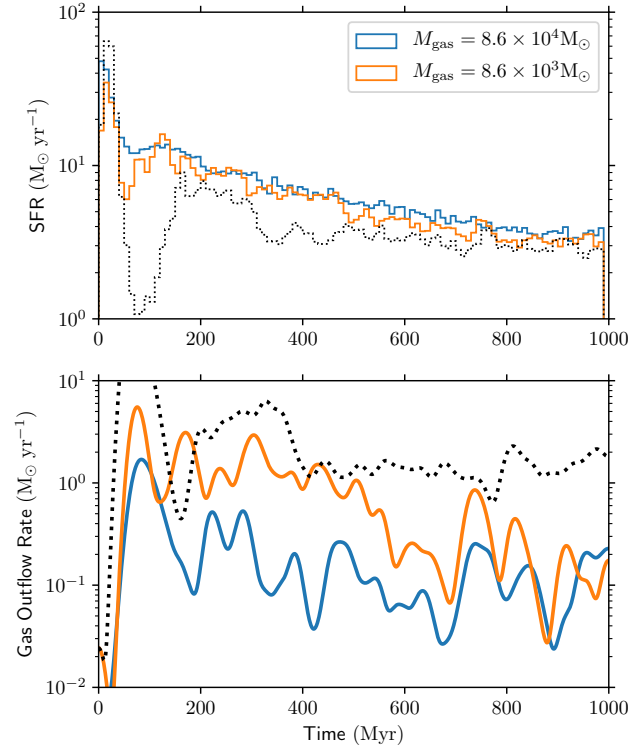


Figure A1. Star formation and outflow rates for galaxies simulated with EMF at our fiducial (orange) and degraded (blue) resolutions. The black dashed curve shows the results of our SN-only galaxy, run at the fiducial resolution. As can be seen, there is a slightly larger burst in at the start of the “settling” phase ($< 50 \text{ Myr}$) at the degraded resolution, as well as somewhat lower outflow rates during the first ~ 2 orbits of the galaxy. For the final $\sim 400 \text{ Myr}$ of the galaxy’s evolution, both the SFR and outflow rates are well converged. As was shown previously, the settled SFR is only slightly increased with the addition of EMF, while the outflow rates are noticeably depressed.

we show the results of galaxies simulated with EMF at the fiducial and degraded resolution, compared to the SN-only case simulated at the fiducial resolution. With degraded resolution, we see a reduction in the mass of the densest gas, in part due to the lowered star formation density threshold (shown as vertical lines in the top panel of Figure A2). Interestingly, we also see a reduction in very hot, diffuse gas, which is in line with what we would expect from the slight reduction in gas outflow rates shown in Figure A1. The differences we see between the two resolution cases are well below the differences between including or omitting EMF. Regardless of resolution, EMF produces significantly less hot, diffuse gas than with SN feedback alone.

APPENDIX B: ROBUSTNESS TO STOCHASTICITY

It has been demonstrated that galaxy evolution is a process that is, at some level, chaotic and stochastic (Keller et al. 2019; Genel et al. 2019). Small-scale perturbations in initial conditions or numerical round-off can produce variations in the overall star formation rate, chemical abundances, and morphological properties of galaxies. Here we demonstrate that the differences we see between our simulations that include EMF and those with SN feedback only are not explained by stochastic variation alone. To this end, we have

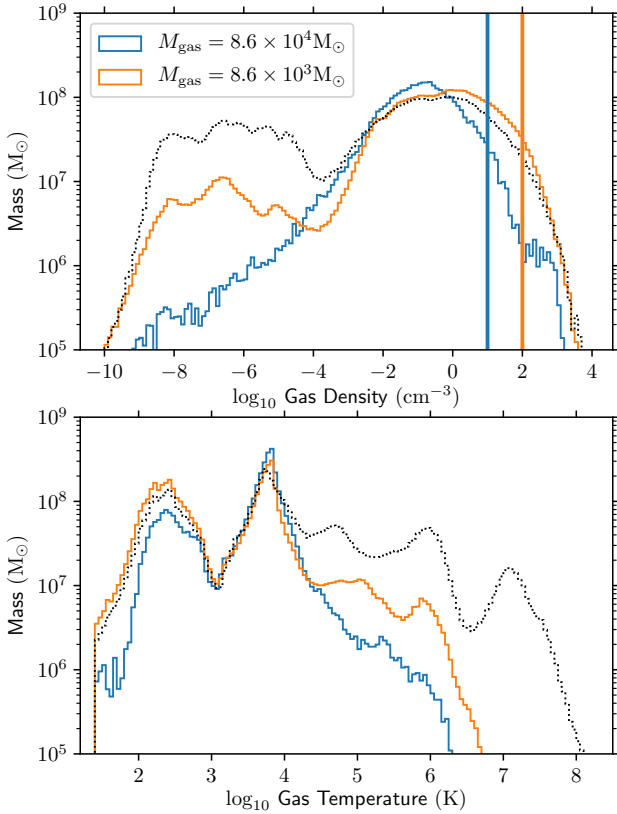


Figure A2. Histograms of density (top panel) and temperature (bottom panel) for our fiducial and degraded resolution. As in Figure A1, the fiducial resolution is shown in orange, the degraded resolution in blue, and the SN-only result in dashed black. In the density histogram, we have annotated the star formation density threshold as the two vertical lines, for the star formation threshold of 10 cm^{-3} and 100 cm^{-3} in the degraded and fiducial simulations respectively. As can be seen, the degraded resolution produces slightly less cold, dense gas ($T < 10^3 \text{ K}$ and $n > 1 \text{ cm}^{-3}$), likely due to the lower star formation threshold as well as the larger gas softening lengths. We also see that the degraded resolution also produces less hot, diffuse gas ($T > 10^5 \text{ K}$ and $n < 10^{-3} \text{ cm}^{-3}$), suggesting that the mechanical SN algorithm is switching to momentum injection mode due to the lower resolution. Despite this, both resolutions with EMF produce less hot, diffuse gas than the SN-only galaxy, and both have roughly equivalent gas in a warm-neutral phase ($T < 10^5 \text{ K}$).

re-simulated both our $\alpha = 1.0$ EMF simulation and the SN-only simulation 8 times, in order to estimate the run-to-run stochasticity in quantities we measure. Because AREPO is fully deterministic, we have introduced a small perturbation into gravity calculations by varying the opening angle θ for gravity calculations (this parameter is given as `ERRTOLTHETA` in AREPO) by $\mathcal{O}(10^{-6})$. This introduces tiny differences in the accelerations calculated by the gravity solver, which can then grow through the mechanisms identified in (Keller et al. 2019). As was shown previously, the expansion exponent α has little impact of EMF, so for these tests we restrict our EMF parameters to the fiducial values of $\alpha = 1$, $p_0 = 375 \text{ km s}^{-1}$, and $t_{\text{FB}} = 3.3 \text{ Myr}$.

In Figure B1, we show the star formation and outflow rates for our stochasticity tests. As in Figure 4, the star formation rates for the SN-only and EMF runs converge after an initial settling period, while the outflow rates diverge to ~ 1 dex differences in the median rates. The scatter in outflow rates is much higher than the

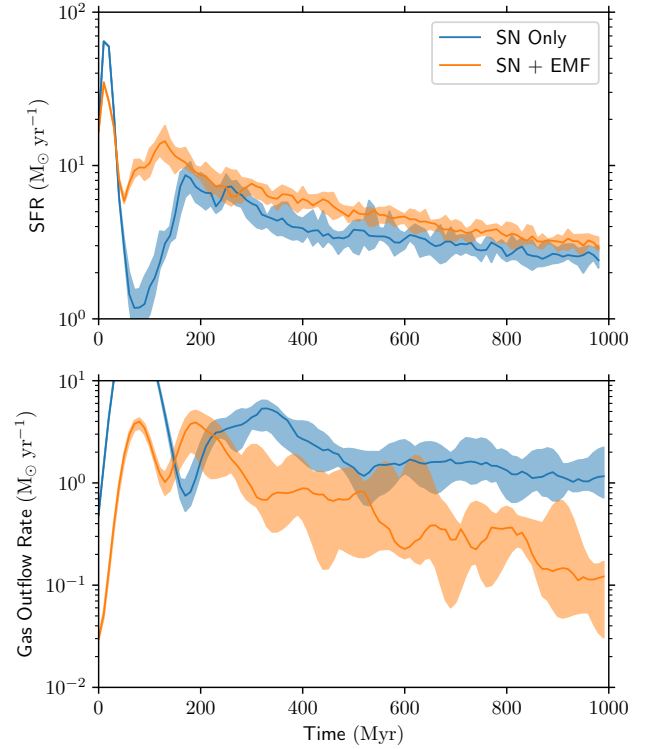


Figure B1. Scatter in star formation (top panel) and outflow (bottom panel) rates for 8 separate runs with infinitesimal perturbations. Blue shaded regions show the range of rates for SN-only runs, while orange shaded regions show the range for SN feedback together with EMF. The solid curve shows the median values. As can be seen, the star formation rates for late times $> 500 \text{ Myr}$ are roughly within the scatter of each other. Outflow rates, while showing larger stochasticity, still show the ~ 1 dex difference in the median rates, consistent with the single runs we examined in the previous sections.

SFR. Keller et al. (2019) showed that temporal stochasticity is a reasonable proxy for run-to-run stochasticity, and the outflow rates we found earlier in Figure 4 show significant temporal variation (burstiness). The larger scatter we see in the outflow rates is consistent with this. Despite the large scatter, the median outflow rates for each feedback mechanism are consistently outside the scatter of the other's run-to-run variation.

Figure B2 shows the variance in gas phase properties. The differences we see between the SN-only runs and the EMF runs are again significant beyond the run-to-run scatter. The scatter in the dense, cool ($< 10^4 \text{ K}$) ISM shows very little stochastic variation, while the hot, diffuse gas shows much larger scatter. Interestingly, the largest scatter occurs in the most thermally-unstable gas, with temperatures between $(10^4 - 10^5 \text{ K})$. As the peak of the solar-metallicity cooling rate curve $\Lambda(T)$ is near 10^5 K , this gas has short cooling times, and is the most transient phase of the gas within the galaxy. Gas colder than this is mostly at the equilibrium temperature (where UV heating matches cooling), while gas hotter than this cools slowly through adiabatic expansion. The gas we see in the intermediate phase is either moving to higher temperatures via SN heating or cooling back to $T < 10^4 \text{ K}$.

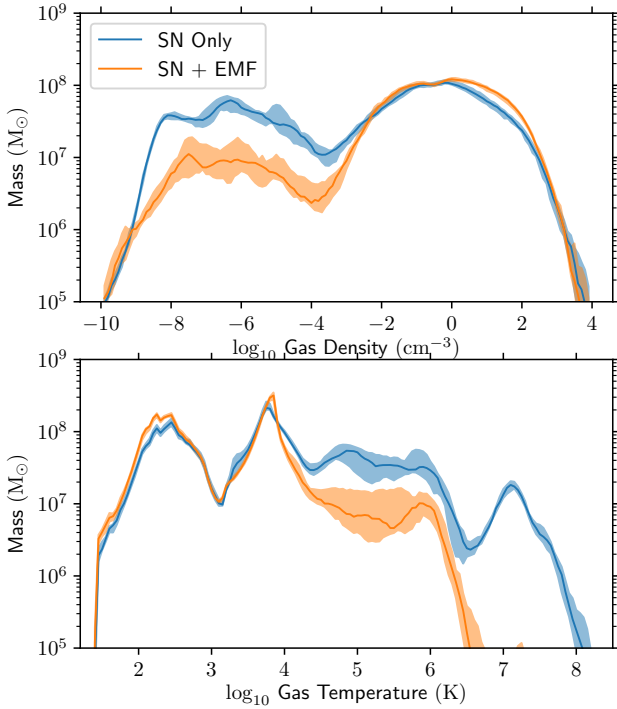


Figure B2. Scatter in gas density (top panel) and temperature (bottom panel) PDFs for 8 perturbed simulations. As in Figure B1, blue regions and lines show results for SN alone, while orange regions and lines show results from including EMF. We can see that the differences between the SN-only runs and those which include EMF are well beyond the run-to-run scatter, primarily in the hottest, most diffuse gas. As this gas is part of a relatively bursty outflow, we see that the scatter in gas above 10^4 K is considerably higher than for cooler neutral/ionized gas.

APPENDIX C: IMPACT OF STAR FORMATION PARAMETERS

In the previous sections, we have restricted our analysis to variations in the parameters and model choices used for stellar feedback. It has been shown that the star formation model, and the parameters used in that model, can also have significant impact on the evolution of the ISM and the galaxy as a whole (e.g. Hopkins et al. 2011; Benincasa et al. 2016; Semenov et al. 2021). In order to probe the relative impact of star formation parameters relative to our new feedback model, we re-simulate our fiducial EMF $\alpha = 1.0$ galaxy while varying the star formation efficiency per free-fall time ϵ_{ff} and the star formation density threshold n_{SF} by a factor of 2 above and below the values used for the other simulations in this paper.

In general, these parameter changes produce little impact on the overall evolution of the galaxy. As we show in Figure C1, both the star formation and outflow rates are within the scatter produced by simple galactic stochasticity shown in Figure B1. Clustering of young stars are also only weakly altered by changing the star formation parameters, as we show in Figure C2. Only in the case where we reduce the star formation threshold density to $n_{\text{SF}} = 50 \text{ cm}^{-3}$ do we see statistically significant differences, with reduced clustering on scales below 100 pc. This is mostly what we would expect, as reducing the threshold density for star formation will allow star forming gas to begin forming stars earlier, when a cloud has not collapsed to the smaller sizes that would be required to reach higher densities. The weak effect we see in the star formation properties also translate to a weak dependence on the star

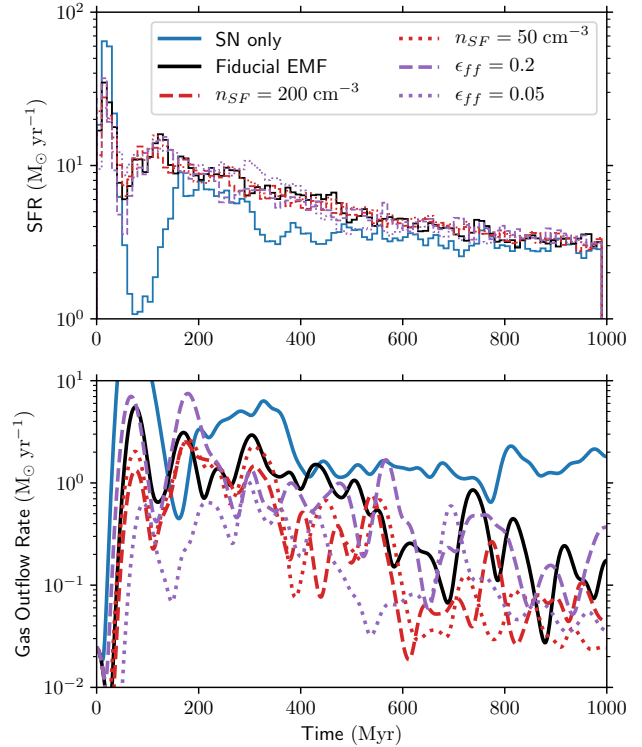


Figure C1. Star formation (top panel) and outflows rates (bottom panel) for galaxies simulated with EMF and different parameters for the star formation efficiency per free-fall time (ϵ_{ff}) and star formation density threshold (n_{SF}). As can be seen, varying either the star formation efficiency or the star formation threshold density does not change the overall star formation rate or the outflow rates beyond the stochasticity we show in Figure B1.

formation parameters for gas properties. In Figure C3, we show the PDFs for gas density and temperature. As can be seen, both quantities show differences within the stochastic scatter shown in Figure B2. The increase in very hot gas ($> 10^7$ K) seen for the $\epsilon_{\text{ff}} = 0.2$ case is the result of a late-time bursty outflow that occurs just before $t = 1$ Gyr, and is not present for the gas temperature PDF from $t = 900$ Myr.

We show the changes to the star formation quantities measured by HEISENBERG in Table C1. As this table shows, we see stronger changes in both the cloud lifetimes t_{gas} and feedback timescale t_{FB} when the star formation threshold density n_{SF} is changed, compared to varying the sub-grid star formation efficiency ϵ_{ff} . As we would expect, lowering ϵ_{ff} results in longer-lived clouds. Lowering n_{SF} pushes the effect in the opposite direction: we find shorter-lived clouds, which are disrupted more quickly, and form a smaller fraction of their mass into stars. A higher star formation threshold requires gas to reach higher densities to form stars: this results in clouds which take longer to begin star formation (and therefore feedback). These denser clouds will also be more difficult to unbind through feedback, which results in a longer feedback timescale. The effects of sub-grid star formation parameters on the spatial decorrelation of dense gas and young stars was explored in Semenov et al. (2021), which also found that the tuning fork diagram is sensitive both to model choices for feedback and star formation. We leave a more comprehensive study of the spatial decorrelation and cloud-scale star formation for star formation, rather than feedback, model choice to a future study.

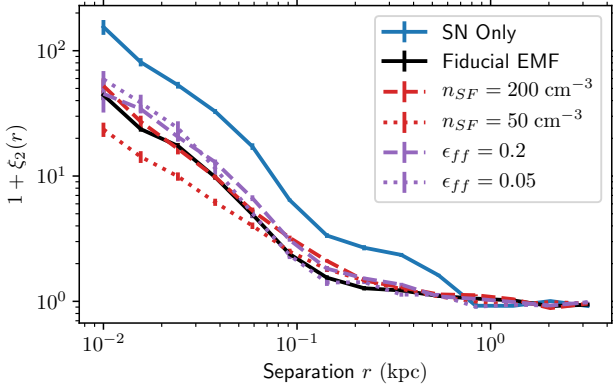


Figure C2. Clustering of young stars as a function of star formation parameters ϵ_{ff} and n_{SF} with EMF. As can be seen, the reduced small-scale clustering of young stars is only slightly altered by changing the star formation parameters, with the largest impact being a slight reduction in the two-point correlation function below 100 pc with a lower density threshold $n_{\text{SF}} = 50 \text{ cm}^{-3}$.

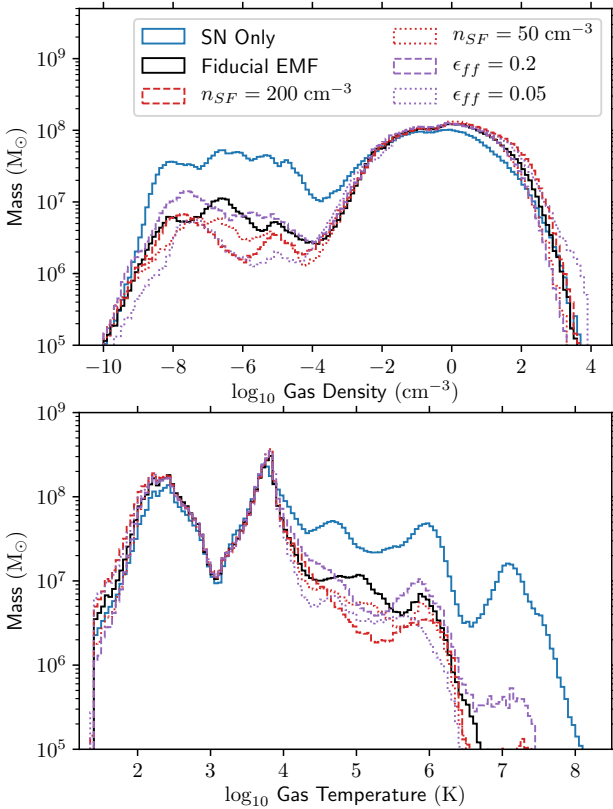


Figure C3. Gas density (top panel) and temperature (bottom panel) PDFs for galaxies simulated with EMF and different star formation parameters. As can be seen, the differences in both the gas temperature and density distributions for different star formation parameters are within the scatter shown in Figure B2.

Galaxy	t_{gas} (Myr)	t_{FB} (Myr)
LMC (observations)	$11.1^{+1.6}_{-1.7}$	$1.1^{+0.3}_{-0.2}$
PHANGS (observations)	$19.8^{+3.0}_{-2.0}$	$3.31^{+0.83}_{-0.76}$
SN Only	$14.8^{+1.7}_{-1.5}$	$3.3^{+0.7}_{-0.7}$
Fiducial EMF	$9.3^{+1.3}_{-0.8}$	$1.4^{+0.6}_{-0.5}$
EMF ($n_{\text{SF}} = 200 \text{ cm}^{-3}$)	$20.4^{+2.2}_{-1.9}$	$2.4^{+0.6}_{-0.6}$
EMF ($n_{\text{SF}} = 50 \text{ cm}^{-3}$)	$4.4^{+0.3}_{-0.4}$	$1.0^{+0.2}_{-0.2}$
EMF ($\epsilon_{\text{ff}} = 0.2$)	$6.6^{+0.9}_{-0.6}$	$1.4^{+0.5}_{-0.6}$
EMF ($\epsilon_{\text{ff}} = 0.05$)	$14.2^{+1.8}_{-1.6}$	$1.1^{+0.5}_{-0.6}$

Table C1. Time-scales and cloud-scale star formation efficiencies measured using HEISENBERG for observations of the LMC and EMF with different sub-grid star formation parameters. As can be seen, increasing the density threshold for star formation increases t_{gas} , and t_{FB} . The same effect occurs when decreasing the subgrid star formation efficiency.

This paper has been typeset from a \LaTeX file prepared by the author.